

The Dilepton-Production Cross Section in Principal Value Resummation

Lyndon Alvero[†] Harry Contopanagos
Institute for Theoretical Physics High Energy Physics Division
SUNY Stony Brook Argonne National Laboratory
Stony Brook, NY 11794-3840 Argonne, IL 60439

August 1995

Abstract

Using a recent calculation of the perturbative hard part for dilepton production that sums large threshold corrections to all orders in perturbative QCD, we compute the corresponding cross sections. The hard part has been evaluated using principal value resummation and contains all singular momentum-dependent corrections. We also include a resummation of large Sudakov terms, which are independent of parton momenta. We give predictions for the dilepton-mass distribution, the rapidity distribution and the rapidity-integrated K -factor at fixed-target energies and compare with various experimental results in several kinematic regimes. We find that principal value resummation produces cross sections that are finite and well-behaved. For both protons and anti-protons on fixed targets, the resummed cross sections are, in general, in excellent agreement with the data.

[†]Present Address: Physics Department, Pennsylvania State University, 104 Davey Lab., University Park, PA 16802-6300

1 Introduction

It is well-known that certain hadron-hadron scattering cross sections, evaluated in perturbative QCD (pQCD), suffer from the presence of large corrections at all but very high energies [1]. These are associated with soft gluons that produce large threshold effects. The primary example of such processes is the dilepton-production cross section, in which the large corrections are associated with the region where all the available partonic momentum is carried away by the dilepton final state. We recently completed the calculation of all these large corrections [2] to all orders in pQCD based on the method of principal value resummation [3], whose main advantage is that it by-passes the infrared (IR) singularities associated with the Landau pole of the QCD running coupling [4]. The corresponding resummed hard part is thus independent of arbitrary IR cutoffs, and can be used to produce unambiguous predictions for the cross section. These are, moreover, stable from a perturbative point of view, since they include *all* such large corrections.

The principal value prescription exponentiates the corrections into a leading and next-to-leading exponent, E_L and E_{NL} , respectively. These exponents contain the effects of the one- (E_L) and two-loop (E_{NL}) running coupling and asymptotically reproduce the resummed perturbative series in the partonic phase space region where perturbation theory is valid. Therefore, the corresponding resummed hard part is well-defined mathematically throughout the whole kinematic region, with all the correct properties associated with perturbation theory. Furthermore, to completely calculate these exponents, which resum the large threshold corrections to all orders in perturbation theory, *only* one- and two-loop calculations of the corresponding hard part are needed. In [3] and [2], we have performed an exhaustive study of the properties of these exponents and the associated resummed hard part in the context of the dilepton cross section. The main objective of the present work is to use this hard part to compare predictions for the physical cross section and related quantities with experiment.

In section 2 we will review the general formulation of the dilepton production cross section, both with the resummed hard part and with finite-order perturbative expressions up to two loops [5]. Our formalism is valid for the differential cross section, with respect to the dilepton invariant mass, as well as for its derivative with respect to rapidity, y , at $y = 0$. In section 3 we review and discuss the resummation of large Sudakov constants [6], which are particularly important as well at low invariant mass. In section 4 we explicitly exhibit the predictions resulting from our formalism, i.e., mass and mass-rapidity (or mass- x_F) distributions and K -factors, and compare these with data from available fixed-target experiments. We will find that principal value resummation produces corrections that are finite and not very large compared to 2-loop corrections. As one goes to higher mass values, the gap between the resummed and finite-order cross sections diminishes. We will also see that the resummation is sensitive to the choice of parton distributions, with global distributions leading to larger cross sections than those obtained from older deep inelastic scattering (DIS) fits. Finally, in section 5 we summarize and discuss our findings. Some numerical details are discussed in an appendix. We postpone comparison with collider experiments to future work.

2 The inclusive cross section for dilepton production

In this section, we review the general formulation for the cross section for dilepton production in hadronic collisions and provide all the necessary formulas for our calculations. This will streamline the discussion which we will give below and facilitate comparisons with various experimental results. For completeness, we present the general formalism for the cross section, valid at either fixed-target or collider energies, even though in this paper we will deal only with the former, i.e., for invariant masses much smaller than the W or Z mass. In the following, we will follow the notation of [7], [8]. In addition, we will also use the notation that for any physical quantity of interest R , R_L stands for this quantity calculated using principal value resummation with the leading exponent E_L only, R for the same resummed quantity using the full exponent $E = E_L + E_{NL}$, while in finite-order pQCD the same quantity will be written as $R_i = \sum_{j=0}^i \alpha^j R^{(j)}$, where $R^{(j)}$ is the j -th order perturbative correction and $\alpha \equiv \alpha_s(Q^2)/\pi$.

In the reaction

$$h_1(p_1) + h_2(p_2) \rightarrow \bar{l}l(Q^\mu) + X, \quad (1)$$

the dilepton pair may be produced by a neutral virtual gauge boson V ($V \in \{\gamma, Z\}$). We will use the standard notation $s = (p_1 + p_2)^2$, $\tau = Q^2/s$, where Q is the dilepton invariant mass.

2.1 Mass distributions and K -factors

We will first deal with the single-differential inclusive cross section

$$\frac{d\sigma^V}{dQ^2} = \sigma_B^V(Q^2)W^V(\tau, Q^2), \quad (2)$$

where σ_B^V is the point-like Born cross section for $q\bar{q} \rightarrow V^* \rightarrow \bar{l}l$ and contains all the electroweak parameters and physical dimensions. In this paper, we are mostly concerned with large perturbative corrections which come from the diagonal-flavor quark-antiquark subprocess. However, when we actually calculate the cross sections, we will also include the contributions coming from the non-singular terms in the 1-loop hard part. Furthermore, we will use parton distribution functions normalized to deep-inelastic scattering experimental data (DIS scheme).

We may now write the hadronic factor as

$$\begin{aligned} W^V(\tau, Q^2) &= \sum_{a,b} C_{ab}^V \int_0^1 \frac{dx_1}{x_1} \frac{dx_2}{x_2} \omega_{ab}(\tau/x_1x_2, \alpha) F_{a/h_1}(x_1, Q^2) F_{b/h_2}(x_2, Q^2) \\ &= \sum_{a,b} C_{ab}^V \int_\tau^1 dz \omega_{ab}(z, \alpha) \frac{\mathcal{F}_{ab}(\tau/z)}{z}, \end{aligned} \quad (3)$$

where the sum extends over all active parton (quark, antiquark and gluon) flavors,

$$\begin{aligned} C_{ff}^\gamma &= C_{fg}^\gamma = C_{gf}^\gamma \equiv C_f^\gamma = e_f^2, \\ C_{ff}^Z &= C_{fg}^Z = C_{gf}^Z \equiv C_f^Z = 1 + (1 - 4|e_f|\sin^2\theta_W)^2, \end{aligned} \quad (4)$$

where e_f is the fractional charge of quark f and θ_W is the electroweak mixing angle. Finally, the parton luminosity is defined as

$$\mathcal{F}_{ab}(\tau/z) = \int_0^1 \delta(1 - \tau/(zx_1x_2)) \frac{dx_1}{x_1} \frac{dx_2}{x_2} F_{a/h_1}(x_1, Q^2) F_{b/h_2}(x_2, Q^2). \quad (5)$$

For our purposes, it is convenient to integrate eq. (3) by parts to obtain the equivalent expression

$$W^V(\tau, Q^2) = \sum_{a,b} C_{ab}^V \int_\tau^1 dz \left[\int_z^1 dz' \omega_{ab}(z', \alpha) \right] \frac{d}{dz} \left(\frac{\mathcal{F}_{ab}(\tau/z)}{z} \right). \quad (6)$$

For the purely electromagnetic case, $V \equiv \gamma$, we have

$$\sigma_B^\gamma(Q^2) = \frac{4\pi\alpha_e^2}{3NQ^2s}, \quad (7)$$

where N is the number of colors and α_e is the (electromagnetic) fine structure constant. Correspondingly, for $V \equiv Z$ we have

$$\sigma_B^Z(Q^2) = \frac{\pi\alpha_e\tau}{4N\sin^2\theta_W\cos^2\theta_WM_Z} \left[\frac{\Gamma_{Z \rightarrow l\bar{l}}}{(Q^2 - M_Z^2)^2 + M_Z^2\Gamma_Z^2} \right], \quad (8)$$

where $M_Z = Z$ boson mass, $\Gamma_{Z \rightarrow l\bar{l}}$ is the partial decay width of Z to one dilepton species,

$$\Gamma_{Z \rightarrow l\bar{l}} = \frac{\alpha_e M_Z (1 + (1 - 4\sin^2\theta_W)^2)}{48\sin^2\theta_W\cos^2\theta_W}, \quad (9)$$

and Γ_Z is the total width of the Z (summed over all leptonic and hadronic decay channels).

The physical cross section $d\sigma/dQ^2$ will in general involve the sum of $d\sigma^V/dQ^2$ over both vector bosons, as well as an interference term, proportional to $\sigma_B^{\gamma Z}$, between the amplitudes mediated by a photon and a Z [7]. For dilepton production in the continuum, i.e., away from resonances, which at fixed-target energies is¹ $Q^2 \ll M_Z^2$, the quantities σ_B^Z , $\sigma_B^{\gamma Z}$ are suppressed relative to σ_B^γ by $(Q/M_Z)^4$ and $(Q/M_Z)^2$, respectively, and therefore we may write

$$\frac{d\sigma}{dQ^2} \simeq \frac{d\sigma^\gamma}{dQ^2}. \quad (10)$$

The K -factor is a quantity that nicely measures the size of the radiative corrections in the hard part by more-or-less cancelling the effect of non-perturbative parton distributions. It may be defined as

$$K \equiv \frac{d\sigma/dQ^2}{d\sigma_0/dQ^2}, \quad (11)$$

where the denominator is calculated in the same way as the numerator, eqs. (2), (3), but using only the tree-level hard part. In the continuum, and in accordance with eq. (10), we may write

$$K \simeq K^\gamma = \frac{d\sigma^\gamma/dQ^2}{d\sigma_0^\gamma/dQ^2} = \frac{W^\gamma(\tau, Q^2)}{W_0^\gamma(\tau, Q^2)}. \quad (12)$$

¹This is the region where all fixed-target experiments are performed since for these experiments, $s < M_Z^2$. For simplicity, we will exclude hadronic resonances, like J/Ψ and Υ , which are subtracted from most experimental data as well.

Since we will only be interested in fixed-target energies, these are the formulas we will use throughout this paper.

We may now obtain resummed expressions for the above quantities by using the resummed hard part ω_{ab} in the above formulas. The expression for the resummed hard part is [2, 3, 9] $\omega_{ab}(z, \alpha) = \delta_{af}\delta_{b\bar{f}}\omega_{f\bar{f}}(z, \alpha)$ with

$$\omega_{f\bar{f}}(z, \alpha) = A(\alpha)I(z, \alpha), \quad (13)$$

where the function $A(\alpha)$ exponentiates the $\delta(1-z)$ terms and will be analysed in detail in section 3, while $I(z, \alpha)$ exponentiates the momentum-dependent plus-distributions that produce large perturbative corrections at the edge of phase space $z \rightarrow 1$. The form of $I(z, \alpha)$ depends on the finite-order structure of the plus-distributions to be resummed and, for best accuracy, should reproduce that structure upon a Taylor expansion in α . In [2] we generically studied $I(z, \alpha)$ using a simplified expression that reproduces *most* of the finite-order large threshold corrections up to two loops and resums *the bulk* of these corrections to all orders. That is sufficient for examining all the properties of the resummation. Since in this work we will compare with experiment, however, we will use a more accurate expression for the hard part, that reproduces *all* of the finite-order large threshold corrections up to two loops and resums them to all orders. Additional resummed structures in $I(z, \alpha)$, that are calculable in principal value resummation [3, 9] and would reproduce, upon expansion, subdominant remaining threshold corrections starting at three-loop order, are negligible. For completeness, we reproduce the expression for $I(z, \alpha)$ below:

$$I(z, \alpha) = \delta(1-z) - \left[\frac{e^E}{(1-z)} \Gamma(1+P_1) Q[P_1, P_2] \right]_+ \quad (14)$$

with

$$Q[P_1, P_2] = \frac{\sin(\pi P_1)}{\pi} \left(1 + P_2 [\Psi^2(1+P_1) + \Psi^{(1)}(1+P_1) - \pi^2] \right) + 2P_2 \cos(\pi P_1) \Psi(1+P_1), \quad (15)$$

where $E = E_L + E_{NL}$ contains all the large logarithmic corrections, Γ is the Euler Gamma function and $\Psi, \Psi^{(1)}$ are the usual polygamma functions, and

$$P_k(x, \alpha) \equiv \frac{\partial^k E(x, \alpha)}{k! \partial x^k}, \quad (16)$$

where it is understood that $E \equiv E(x, \alpha)$ is a function that has a polynomial representation in $x \equiv \ln(1/(1-z))$ and α in the perturbative regime. From eqs. (6), (13) and (14), we may eliminate the δ -function and plus-distributions by explicitly integrating the former and using the property $\int_z^1 dz' [f(z')]_+ = -\int_0^z dz' f(z')$ for the latter. Hence, our final form for the resummed hadronic function is

$$W^V(\tau, Q^2) = \sum_f C_f^V A(\alpha) \int_\tau^1 dz [1 + \mathcal{H}(z, \alpha)] \frac{d}{dz} \left(\frac{\mathcal{F}_{f\bar{f}}(\tau/z)}{z} \right), \quad (17)$$

where the function $\mathcal{H}(z, \alpha)$ is given by

$$\mathcal{H}(z, \alpha) \equiv \int_0^{\ln(\frac{1}{1-z})} dx e^{E(x, \alpha)} \Gamma(1+P_1(x, \alpha)) Q[P_1(x, \alpha), P_2(x, \alpha)]. \quad (18)$$

It will also be of interest to compare the resummed expression for the cross section or the K -factor with the corresponding quantities obtained from finite-order calculations. The corresponding hadronic factor is given by

$$W_i^V(\tau, Q^2) = \sum_{a,b} C_{ab}^V \int_{\tau}^1 dz \left[\int_z^1 dz' \omega_{ab}^i(z', \alpha) \right] \frac{d}{dz} \left(\frac{\mathcal{F}_{ab}(\tau/z)}{z} \right), \quad (19)$$

where the finite-order perturbative hard part is denoted by

$$\omega_{ab}^i(z, \alpha) = \sum_{j=0}^i \alpha^j \omega_{ab}^{(j)}(z). \quad (20)$$

The corresponding finite-order mass-distribution and K -factor are given by

$$\frac{d\sigma_i^V}{dQ^2} = \sigma_B^V(Q^2) W_i^V(\tau, Q^2) \quad \text{and} \quad K_i^V = \frac{W_i^V(\tau, Q^2)}{W_0^V(\tau, Q^2)}. \quad (21)$$

The hard part $\omega_{f\bar{f}}^i$ has been calculated up to second order in both DIS and $\overline{\text{MS}}$ schemes, in [5]-[11], and [7], respectively. The full two-loop corrections are quite lengthy but the leading corrections, as in the one-loop case [13], are the ‘‘singular’’ ones in the $z \rightarrow 1$ limit, i.e., the ones that are proportional to a delta function or a plus distribution. These come from virtual and soft-gluon corrections and are only present in the $q\bar{q}$ channel of the initial partons. We reproduce these corrections in the DIS scheme below, together with the leading order hard part:

$$\omega_{ab}^{(0)} = \delta_{af} \delta_{b\bar{f}} \delta(1-z), \quad (22)$$

$$\omega_{f\bar{f}}^{(1)} = \frac{C_F}{2} \left(2(1+z^2)\mathcal{D}_1(z) + 3\mathcal{D}_0(z) + \left(1 + \frac{4}{3}\pi^2\right)\delta(1-z) - 4z - 6 \right), \quad (23)$$

$$\omega_{fg}^{(1)} = \omega_{g\bar{f}}^{(1)} = \frac{C_F}{2} \frac{3}{8} \left(\left[z^2 + (1-z)^2 \right] \ln(1-z) + \frac{9}{2}z^2 - 5z + \frac{3}{2} \right), \quad (24)$$

$$\begin{aligned} \omega_{f\bar{f}}^{(2)} \simeq & \frac{1}{16} \left\{ C_F^2 \left(32\mathcal{D}_3(z) + 72\mathcal{D}_2(z) + [64\zeta(2) + 52]\mathcal{D}_1(z) + [112\zeta(3) + 24\zeta(2) + 15]\mathcal{D}_0(z) \right) \right. \\ & + C_A C_F \left(-44\mathcal{D}_2(z) + \left[\frac{338}{9} - 16\zeta(2) \right] \mathcal{D}_1(z) + \left[57 + \frac{88}{3}\zeta(2) - 24\zeta(3) \right] \mathcal{D}_0(z) \right) \\ & + n_f C_F \left(8\mathcal{D}_2(z) - \frac{44}{9}\mathcal{D}_1(z) - \left[10 + \frac{16}{3}\zeta(2) \right] \mathcal{D}_0(z) \right) \\ & + \delta(1-z) \left(C_F^2 \left[\frac{548}{5}\zeta(2)^2 + 120\zeta(3) - 3\zeta(2) \right] \right. \\ & + C_A C_F \left[\frac{215}{9} + \frac{2098}{9}\zeta(2) - \frac{196}{3}\zeta(3) - \frac{154}{5}\zeta(2)^2 \right] \\ & \left. \left. + n_f C_F \left[\frac{16}{3}\zeta(3) - \frac{340}{9}\zeta(2) - \frac{38}{9} \right] \right) \right\}, \quad (25) \end{aligned}$$

where $\zeta(s)$ is the Riemann Zeta function and

$$\mathcal{D}_i(z) = \left[\frac{\ln^i(1-z)}{1-z} \right]_+. \quad (26)$$

The \simeq in eq. (25) signifies that we have dropped all terms that are non-singular in the $z \rightarrow 1$ -limit. This, of course, raises the question of how dominant the above singular terms are relative to the non-singular ones, that occur both in the $q\bar{q}$ channel and in the other initial-parton-state channels, or conversely, how important are the contributions due to the non-singular terms. A thorough numerical investigation of this issue has already been conducted [7, 10, 11]. The conclusions vary depending somewhat on the factorization scheme, and on the range of energy and invariant mass.² We may say, in general, that at fixed-target energies, the 2-loop non-singular terms account for no more than a 10% *negative* contribution to the exact mass distribution over all channels, with the approximation improving as τ increases. For details regarding variations of this result with the order, the factorization scheme, etc., see [11]. Relative to the resummed cross section then, the 2-loop non-singular terms would only lead to a 3 to 7% reduction. Given these general remarks, and because of the complicated structure of the 2-loop non-singular contributions, we did not include them in our cross section calculations but we should bear in mind the reduction that they would induce in our resummed predictions. As a last note, the terms proportional to $\delta(1-z)$ in eqs. (23) and (25), will also be useful in determining the factor $A(\alpha)$ in eq. (13), as will be shown in section 3.

2.2 Differential mass distributions

We can also use principal value resummation to compute the rapidity distribution of dileptons in the central rapidity region. This is possible because the rapidity, or any other smooth function of the vector boson momentum, when in the central region and expressed in terms of the initial- and final-state momenta, is approximated by a function of the initial parton momenta with corrections that are suppressed by vanishing final-state phase space [12]. To be specific, it has been shown in [12] that for any kinematic variable $\bar{\eta}$ which is a smooth function of the vector boson momentum, the resummed quantity $d^2\sigma^V/dQ^2d\bar{\eta}$ is approximated by

$$\begin{aligned} \frac{d^2\sigma^V}{dQ^2d\bar{\eta}}(\tau, Q^2, \bar{\eta}) &\simeq \sigma_B^V \sum_f C_f^V \int_0^1 \frac{dx_1}{x_1} \frac{dx_2}{x_2} \omega_{f\bar{f}}(\tau/x_1x_2, \alpha) F_{f/h_1}(x_1, Q^2) F_{\bar{f}/h_2}(x_2, Q^2) \\ &\times \delta(\bar{\eta} - \eta(x_1p_1, x_2p_2)) \equiv \frac{d^2\widetilde{\sigma}^V}{dQ^2d\bar{\eta}}(\tau, Q^2, \bar{\eta}), \end{aligned} \quad (27)$$

where $\omega_{f\bar{f}}(z, \alpha)$ is given by eq. (13) and $\eta(x_1p_1, x_2p_2)$ denotes the corresponding parton-model expression. By analogy to eqs. (3) and (6), we can re-write eq. (27) as

$$\frac{d^2\widetilde{\sigma}^V}{dQ^2d\bar{\eta}}(\tau, Q^2, \bar{\eta}) \simeq \sigma_B^V \sum_f C_f^V \int_\tau^1 dz \left[\int_z^1 dz' \omega_{f\bar{f}}(z', \alpha) \right] \frac{d}{dz} \left(\frac{\mathcal{F}_{f\bar{f}}^{\bar{\eta}}(\tau/z)}{z} \right), \quad (28)$$

where

$$\mathcal{F}_{f\bar{f}}^{\bar{\eta}}(\tau/z) \equiv \int_0^1 \frac{dx_1}{x_1} \frac{dx_2}{x_2} \delta \left(1 - \frac{\tau/z}{x_1x_2} \right) \delta(\bar{\eta} - \eta(x_1p_1, x_2p_2)) F_{f/h_1}(x_1) F_{\bar{f}/h_2}(x_2). \quad (29)$$

²In fact, for the mass-distribution, the question can be fully answered up to two loops, given the recent work of [11]. This is not so for the differential mass distribution, described in sec. 2.2, since the full two-loop results are not available at present.

If we choose the kinematical variable $\bar{\eta}$ to be the rapidity y ,

$$\bar{\eta} \equiv y = \frac{1}{2} \ln \left(\frac{q_0 + q_L}{q_0 - q_L} \right), \quad (30)$$

we obtain for the partons

$$y(x_1 p_1, x_2 p_2) = \frac{1}{2} \ln \left(\frac{x_1}{x_2} \right), \quad (31)$$

so that at $y = 0$,

$$\frac{d^2 \sigma^V}{dQ^2 dy}(\tau, Q^2, y = 0) \simeq \sigma_B^V W_{y=0}^V(\tau, Q^2), \quad (32)$$

where

$$W_{y=0}^V(\tau, Q^2) = \sum_f C_f^V A(\alpha) \int_\tau^1 dz [1 + \mathcal{H}(z, \alpha)] \frac{d}{dz} \left(\frac{\mathcal{F}_{f\bar{f}}^{y=0}(\tau/z)}{z} \right), \quad (33)$$

with

$$\mathcal{F}_{f\bar{f}}^{y=0}(\tau/z) = F_{f/h_1} \left(\sqrt{\tau/z} \right) F_{\bar{f}/h_2} \left(\sqrt{\tau/z} \right). \quad (34)$$

Similarly, choosing $\bar{\eta}$ to be the Feynman parameter x_F ,

$$\bar{\eta} \equiv x_F \equiv 2q_L/\sqrt{s}, \quad (35)$$

where q_L is the longitudinal momentum of the virtual vector boson in the center-of-mass frame of the hadrons, we have³

$$x_F(x_1 p_1, x_2 p_2) = x_1 - x_2. \quad (36)$$

Therefore the resummed double-differential distribution at $x_F = 0$ is

$$\frac{d^2 \sigma^V}{dQ^2 dx_F}(\tau, Q^2, x_F = 0) \simeq \sigma_B^V(Q^2) W_{x_F=0}^V(\tau, Q^2), \quad (37)$$

where $W_{x_F=0}^V$ is given by eq. (33), with the substitution

$$\mathcal{F}^{y=0}(\tau/z) \rightarrow \mathcal{F}^{x_F=0}(\tau/z) = \frac{1}{2\sqrt{\tau/z}} F_{f/h_1} \left(\sqrt{\tau/z} \right) F_{\bar{f}/h_2} \left(\sqrt{\tau/z} \right). \quad (38)$$

Finite-order approximations can also be written down in a similar way:

$$\frac{d^2 \sigma^{V,i}}{dQ^2 d\bar{\eta}}(\tau, Q^2, \bar{\eta}) \simeq \frac{d^2 \widetilde{\sigma}^{V,i}}{dQ^2 d\bar{\eta}}(\tau, Q^2, \bar{\eta}) \equiv \sigma_B^V(Q^2) W_{\bar{\eta}}^{V,i}(\tau, Q^2), \quad (39)$$

with

$$W_{\bar{\eta}}^{V,i}(\tau, Q^2) = \sum_{a,b} C_{ab}^V \int_\tau^1 dz \left[\int_z^1 dz' \omega_{ab}^i(z', \alpha) \right] \frac{d}{dz} \left(\frac{\mathcal{F}_{ab}^{\bar{\eta}}(\tau/z)}{z} \right), \quad (40)$$

³In actual experiments, x_1 typically corresponds to the momentum fraction of a parton in the beam hadron while x_2 corresponds to that of a parton in the target hadron.

where $\bar{\eta} = y$ or x_F and $\omega_{ab}^i(z', \alpha)$ is given by eqs. (22)-(25).

We illustrate the accuracy of the approximation (27) in two ways. First, we compare in fig. 1 the full $\mathcal{O}(\alpha)$ distribution (i.e., all 1-loop non-singular terms in the hard part are included) using eq. (39) (with $i = 1$) and the exact distribution derived in [13], in the central region. The kinematic parameters used are taken from the Fermilab E605 experiment [19] and are described in section 4. The solid curve is the exact one-loop calculation while the dotted curve is the corresponding approximation. We see that the approximation is not perfect, with about a 10% difference between the two curves. This difference comes mostly from the quark-gluon channel. Hence, in all our subsequent calculations for double differential distributions, we used the exact results of [13] for the quark-gluon channel alone. The remaining error is then of order 1%, which shows that the general approximation (eq. (27)) for the channel containing the singular corrections is indeed very good.

In most experiments, what is measured is not the fully integrated mass distribution $d\sigma/dQ^2$ but instead one that is *partially* integrated over either the rapidity y or x_F in some kinematic range $\mathcal{R}(\tau)$. In order to compare with actual experimental data, we use the following approximation

$$\left(\frac{d\sigma^V}{dQ^2}\right)_{\bar{\eta} \in \mathcal{R}(\tau)} \equiv \int_{\bar{\eta} \in \mathcal{R}(\tau)} d\bar{\eta} \frac{d^2\sigma^V}{dQ^2 d\bar{\eta}} \simeq \int_{\bar{\eta} \in \mathcal{R}(\tau)} d\bar{\eta} \frac{\widetilde{d^2\sigma^V}}{dQ^2 d\bar{\eta}} = \sigma_B^V(Q^2) W_{\bar{\eta} \in \mathcal{R}(\tau)}^V(\tau, Q^2), \quad (41)$$

with $\widetilde{d^2\sigma^V}/dQ^2 d\bar{\eta}$ given by eq. (27) so that $W_{\bar{\eta} \in \mathcal{R}(\tau)}^V(\tau, Q^2)$ is given by eq. (33) with the substitution

$$\begin{aligned} \mathcal{F}_{f\bar{f}}^{y=0}(\tau/z) &\rightarrow \mathcal{F}_{f\bar{f}}^{\bar{\eta}}(\tau/z) \equiv \int_{\bar{\eta} \in \mathcal{R}(\tau)} d\bar{\eta} \int_0^1 \frac{dx_1}{x_1} \frac{dx_2}{x_2} \delta\left(1 - \frac{\tau/z}{x_1 x_2}\right) \\ &\quad \times \delta(\bar{\eta} - \eta(x_1 p_1, x_2 p_2)) F_{f/h_1}(x_1) F_{\bar{f}/h_2}(x_2). \end{aligned} \quad (42)$$

The second way, therefore, that we will test eq. (27) is by comparing eq. (41) in finite-order pQCD with an exact calculation at the end of this section.

The integrals over x_1, x_2 in eq. (42) are trivial to perform. Let us first consider the case of $\bar{\eta} \equiv x_F$ with $\mathcal{R}(\tau)$ the positive kinematic range $(0, 1 - \tau)$, as is the case for most experiments. We will denote the corresponding function in eq. (42) by $\mathcal{F}_{f\bar{f}}^{x_F > 0}$. Notice that upon performing the integrations over the parton fractions, the constraints $x_1 - x_2 = x_F$ and $x_1 x_2 = \tau/z$ transform the positive kinematic range of x_F into $(0, 1 - \tau/z)$, which makes the function $\mathcal{F}_{f\bar{f}}^{x_F > 0}$ depend on the scaling variable τ/z only. We obtain the result

$$\mathcal{F}_{f\bar{f}}^{x_F > 0}(\tau/z) = \int_0^{1-\frac{\tau}{z}} \frac{dx_F}{\sqrt{x_F^2 + 4\tau/z}} F_{f/h_1}\left(\frac{x_F + \sqrt{x_F^2 + 4\tau/z}}{2}\right) F_{\bar{f}/h_2}\left(\frac{-x_F + \sqrt{x_F^2 + 4\tau/z}}{2}\right). \quad (43)$$

On the other hand, if $\bar{\eta} \equiv y$ and we want an analogous expression which holds for $y > 0$, the corresponding constraints are $y = \frac{1}{2} \ln(x_1/x_2)$ and $x_1 x_2 = \tau/z$ so that we get ⁴

⁴Note that $x_F > 0$ implies $y > 0$ and vice-versa, and in fact using either x_F or y for representing the differential mass distribution amounts to a change of integration variable, so that eqs. (43) and (44) give identical results. We found it convenient to use eq. (44) for calculating the y (or x_F) > 0 cross sections.

$$\mathcal{F}_{f\bar{f}}^{y>0}(\tau/z) = \int_0^{\frac{1}{2}\ln(\frac{z}{\tau})} dy F_{f/h_1} \left(\sqrt{\frac{\tau}{z}} e^y \right) F_{\bar{f}/h_2} \left(\sqrt{\frac{\tau}{z}} e^{-y} \right). \quad (44)$$

Summarizing these results, we write

$$\left(\frac{d\sigma^V}{dQ^2} \right)_{\bar{\eta}>0} \simeq \sigma_B^V(Q^2) W_{\bar{\eta}>0}^V(\tau, Q^2), \quad (45)$$

where

$$W_{\bar{\eta}>0}^V(\tau, Q^2) = \sum_f C_f^V A(\alpha) \int_\tau^1 dz [1 + \mathcal{H}(z, \alpha)] \frac{d}{dz} \left(\frac{\mathcal{F}_{f\bar{f}}^{\bar{\eta}>0}(\tau/z)}{z} \right). \quad (46)$$

Finite-order approximations take a similar form:

$$\left(\frac{d\sigma^{V,i}}{dQ^2} \right)_{\bar{\eta}>0} \simeq \sigma_B^V(Q^2) W_{\bar{\eta}>0}^{V,i}(\tau, Q^2), \quad (47)$$

with $W_{\bar{\eta}>0}^{V,i}(\tau, Q^2)$ given by eq. (40) but with $\mathcal{F}_{ab}^{\bar{\eta}=0}(\tau/z)$ replaced by $\mathcal{F}_{ab}^{\bar{\eta}>0}(\tau/z)$, eq. (42).

In fig. 2 we test the approximation shown in eq. (41) by again comparing the resulting partially integrated distribution, $\left(\frac{d\sigma^V}{dQ^2} \right)_{y>0}$, with the exact one using the results of [13]. The calculations were done to one loop order, and the comparison is made within the context of the E772 experiment, with kinematics that we will describe in sec. 4. We see that in this case, the approximation works very well.

In section 4 we will use these formulas in presenting our predictions and comparisons with various fixed-target experiments.

3 The function $A(\alpha)$

We now turn to the coefficient function $A(\alpha)$ in eq. (13), which is closely connected to the Sudakov form factor. In [4], this function was given to $\mathcal{O}(\alpha)$ in the exponent as:

$$A_1(\alpha) = (1 + 2C_F\alpha) \exp \left[\frac{\alpha}{2} C_F \left(\frac{4}{3}\pi^2 - 3 \right) \right]. \quad (48)$$

In this expression, the piece $\frac{\alpha}{2} C_F \pi^2$ of the exponent is identified with the absolute value squared of the ratio of the Sudakov form factor at timelike and spacelike momentum transfer, $\Gamma(Q^2)/\Gamma(-Q^2)$.

To obtain an $\mathcal{O}(\alpha^2)$ form of $A(\alpha)$, we use eq. (3.8) of [6]:

$$\begin{aligned} \ln \frac{\Gamma(Q^2)}{\Gamma(-Q^2)} &= i\frac{\pi}{2} \left[\alpha K^{(1)} + \alpha^2 K^{(2)} \right] + \frac{G^{(1)}}{2b_2} \ln \nu + \frac{G^{(2)}}{2b_2} \alpha \left(1 - \frac{1}{\nu} \right) \\ &\quad - \frac{\gamma_K^{(1)}}{4b_2^2} \frac{1}{\alpha} (\nu \ln \nu - \nu + 1) + \frac{\gamma_K^{(2)}}{4b_2^2} (\ln \nu - \nu + 1) \end{aligned} \quad (49)$$

where

$$\begin{aligned}
b_2 &= \frac{11}{12}C_A - \frac{2}{12}n_f, \\
\nu &= 1 + i\pi b_2\alpha, \\
\gamma_K^{(1)} &= 2C_F, \\
\gamma_K^{(2)} &= C_A C_F \left[\frac{67}{18} - \zeta(2) \right] - \frac{5}{9}n_f C_F.
\end{aligned} \tag{50}$$

The $\gamma_K^{(i)}$'s are anomalous dimension coefficients.

It is sufficient to consider only the real part of eq. (49):

$$\text{Re} \left[\ln \frac{\Gamma(Q^2)}{\Gamma(-Q^2)} \right] = \frac{G^{(1)}}{2b_2} \ln r + \frac{\pi G^{(2)}}{2} \frac{\sin \theta}{r} \alpha^2 - \frac{\gamma_K^{(1)}}{4b_2^2} \frac{1}{\alpha} (\ln r - \pi b_2 \theta \alpha) + \frac{\gamma_K^{(2)}}{4b_2^2} \ln r, \tag{51}$$

where

$$r = \left[1 + (\pi b_2 \alpha)^2 \right]^{\frac{1}{2}}, \quad \theta = \arctan(\pi b_2 \alpha). \tag{52}$$

The constant $G^{(1)}$ is obtained from eq. (2.7) of [6],

$$G^{(1)} = \frac{3}{2}C_F, \tag{53}$$

while the constant $G^{(2)}$ can be found from their eqs. (4.1), (4.2), (4.3), (2.5) and (2.6)⁵:

$$\begin{aligned}
G^{(2)} &= C_F^2 \left[\frac{3}{16} - \frac{7}{3}\zeta(3) + \frac{23}{6}\zeta(2) \right] + C_A C_F \left[\frac{2545}{432} + \frac{11}{12}\zeta(2) - \frac{13}{4}\zeta(3) \right] \\
&\quad + n_f C_F \left[-\frac{209}{216} - \frac{1}{6}\zeta(2) \right].
\end{aligned} \tag{54}$$

Expanding eq. (51) up to $\mathcal{O}(\alpha^2)$, one obtains the exponentiated result

$$\left| \frac{\Gamma(Q^2)}{\Gamma(-Q^2)} \right|^2 = \exp \left(\frac{\alpha}{2} C_F \pi^2 + \frac{\alpha^2}{16} \pi^2 \left[\left(\frac{233}{9} - \frac{2}{3} \pi^2 \right) C_A C_F - \frac{38}{9} n_f C_F \right] \right). \tag{55}$$

The $\mathcal{O}(\alpha^2)$ exponentiated function $A(\alpha)$ can now be written as

$$\begin{aligned}
A_2(\alpha) &= \left(1 + 2C_F \alpha + b\alpha^2 \right) \exp \left(\frac{\alpha}{2} C_F \left[\frac{4}{3} \pi^2 - 3 \right] \right. \\
&\quad \left. + \frac{\alpha^2}{16} \pi^2 \left[\left(\frac{233}{9} - \frac{2}{3} \pi^2 \right) C_A C_F - \frac{38}{9} n_f C_F \right] \right).
\end{aligned} \tag{56}$$

The constant b is determined by expanding eq. (56) in α and then comparing the result with the terms proportional to $\delta(1-z)$ in the second-order result $\omega_{ff}^{(2)}$, eq. (25). This yields

$$\begin{aligned}
b &= C_F^2 \left[\frac{-23}{720} \pi^4 - \frac{35}{96} \pi^2 + \frac{15}{2} \zeta(3) + \frac{15}{8} \right] + C_A C_F \left[\frac{215}{144} + \frac{175}{216} \pi^2 - \frac{49}{12} \zeta(3) - \frac{17}{1440} \pi^4 \right] \\
&\quad + n_f C_F \left[\frac{1}{3} \zeta(3) - \frac{19}{72} - \frac{7}{54} \pi^2 \right].
\end{aligned} \tag{57}$$

⁵There is a misprint in eq. (4.3) of [6]. The right-hand side of the equation should read $-4\epsilon\Gamma_2^{(2)} \left[\frac{\mu^2}{-q^2} \right]^{2\epsilon} - 2\epsilon\Gamma_1^{(2)} \left[\frac{\mu^2}{-q^2} \right]^\epsilon - (K^{(1)} + G^{(1)})\Gamma^{(1)}$.

There is yet another way of treating the function $A(\alpha)$. The accuracy of the expansion of eq. (51) actually depends on the size of $\pi b_2 \alpha$. Given the value of $b_2 = 2.0833$ at $n_f = 4$, one can easily check that $\pi b_2 \alpha$ is not really a very small number. Thus, instead of expanding in α , one can use the exact expression in eq. (51) to obtain the following expression for $A(\alpha)$:⁶

$$A(\alpha) = \left(1 + 2C_F \alpha + b\alpha^2\right) \exp\left(\frac{\alpha}{2} C_F \left[\frac{\pi^2}{3} - 3\right] + \frac{G^{(1)}}{b_2} \ln r + \pi G^{(2)} \frac{\sin \theta}{r} \alpha^2 + \frac{\gamma_K^{(1)}}{2b_2^2} \frac{1}{\alpha} (\pi b_2 \theta \alpha - \ln r) + \frac{\gamma_K^{(2)}}{2b_2^2} \ln r\right). \quad (58)$$

Note that at high energies, eq. (55) becomes a good enough approximation to eq. (51) so that the constant b in eq. (58) is the same b that appears in eq. (56), given explicitly by eq. (57).

In fig. 3 we have plotted the different forms $A_1(\alpha)$, $A_2(\alpha)$ and $A(\alpha)$ for $n_f = 4$ and $\Lambda = 0.25\text{GeV}$. For consistency, we have used the two-loop form of α for $A_2(\alpha)$ and $A(\alpha)$ and a one-loop α for $A_1(\alpha)$. One sees that the following relation holds: $A(\alpha) > A_2(\alpha) > A_1(\alpha)$ where $A(\alpha)$ is given by eq. (58), $A_2(\alpha)$ by eq. (56) and $A_1(\alpha)$ by eq. (48). As Q increases, all three functions become numerically close to 1, as expected from asymptotic freedom. On the other hand, at low values of Q all three functions have large numerical values, and diverge as Q approaches the confinement scale. In the mass-range of fixed-target experiments, all three forms of A are numerically very similar to one another. In the following section we will give predictions for the resummed dilepton cross section using only the exact, $\mathcal{O}(\alpha^2)$ function $A(\alpha)$.

4 Comparisons with experiment

4.1 Generalities

In this section, we present our numerical calculations and compare them with results from several fixed-target experiments. To be consistent with the two-loop running coupling used in the calculation of the resummed exponent [2], we use the following two-loop form of α in terms of Λ :

$$\alpha(Q^2) \equiv \frac{\alpha_s(Q^2)}{\pi} = \frac{1}{b_2 \ln(Q^2/\Lambda^2)} - \frac{b_3 \ln(\ln(Q^2/\Lambda^2))}{b_2^2 \ln^2(Q^2/\Lambda^2)}, \quad (59)$$

with

$$b_2 = (11C_A - 2n_f)/12, b_3 = (34C_A^2 - (10C_A + 6C_F)n_f)/48. \quad (60)$$

For parton distributions, we used the recent CTEQ2D [14] and MRSD- [15] parton sets that are based on global fits. In the hard part, we used the Λ_{n_f} values provided with the appropriate parton distribution. The parameter n_f is either 4 or 5 depending on the value of Q at which the parton density is evaluated.

We note here that in all the discussions to follow, by resummed cross section, we mean the resummed cross section obtained from eq. (32) or (45) plus the contributions of all the

⁶ In the following, it is this “exact” expression that we will denote by $A(\alpha)$ and use in the numerical computations.

non-singular terms in the 1-loop hard part, $\omega_{ab}^{(1)}(z, \alpha)$. Specifically, these are $\alpha\omega_{fg}^{(1)}$ (eq. (24)) and $\alpha\frac{C_F}{2}(-4z - 6 + 2(1 - z)\ln(1 - z) - 4\ln(1 - z))$, derivable from $\alpha\omega_{ff}^{(1)}$ of eq. (23).

4.2 The NA3 (1980) Experiment

This experiment [16] involved the hadronic production of dimuons from the interaction of a proton- ($\sqrt{s} = 19.4\text{GeV}$) and anti-proton- beam ($\sqrt{s} = 16.8\text{GeV}$) with a platinum (Pt) target. In fig. 4a we have plotted the data points together with the one-loop, two-loop and resummed forms of the mass distribution $M_{\mu\mu}^3 \frac{d\sigma}{dM_{\mu\mu}} \Big|_{x_F > 0}$ using the CTEQ2D ($\Lambda_4 = 0.235\text{GeV}$) distribution. For both $p-$ and $\bar{p}-$ on Pt, all three curves exhibit acceptable agreement with data.

We show in fig. 4b the resulting curves using the MRSD- ($\Lambda_4 = 0.23\text{GeV}$) parton set. For \bar{p} on Pt, the curves are almost identical to the corresponding ones in fig. 4a, while the p on Pt curves are slightly higher than their CTEQ2D counterparts. These suggest that CTEQ2D and MRSD- have almost the same valence quarks but slightly different sea quark parametrizations.

It should be noted here that the size of the resummed cross sections is largely determined by the function $A(\alpha)$. In fig. 5, by looking at the dotted (Born) and dashed (resummed but with $A(\alpha)$ replaced by 1) curves, we note that the contribution of the plus distributions steadily increases with $\sqrt{\tau}$, from only a few percent in the range $\sqrt{\tau} \leq 0.3$, up to about 26% at $\sqrt{\tau} \simeq 0.5$. Comparing the dashed curve with the solid one, we can also determine that the plus distributions contribute from only a few percent to about 11%, in the same regions of $\sqrt{\tau}$, to the resummed cross section. One can also check that, in the mass range of this plot, at least 80% of the resummed cross section comes from $A(\alpha) \times$ Born cross section.

4.3 The NA3 (1985) Experiment

In this experiment [17], dimuon events, at $\sqrt{s} = 27.4\text{ GeV}$, produced in the collisions of protons with a platinum (Pt) target, and within the range $x_F > 0$ were analyzed.

In fig. 6 we present our resummed prediction for the mass distribution $M_{\mu\mu}^3 \frac{d\sigma}{dM_{\mu\mu}} \Big|_{x_F > 0}$, using the CTEQ2D ($\Lambda_4 = 0.235\text{GeV}$) parton set. The resummed curve is no more than 23% above the data, and the 1-loop prediction fits the data best.

4.4 The E537 Experiment

This Fermilab experiment [18] involved collisions of an antiproton beam with a tungsten (W) target at $\sqrt{s} = 15.4\text{ GeV}$. Again, dimuon production events which fell in the positive x_F -range were selected.

In fig. 7, we have plotted the data points and the mass distribution $M_{\mu\mu}^3 \frac{d\sigma}{dM_{\mu\mu}} \Big|_{x_F > 0}$, using the CTEQ2D parton distribution. Here, the resummed curve has the best fit. The 2-loop curve also has a good fit but with a slight underestimate.

We have also plotted the differential mass distribution $M^3 \frac{d^2\sigma}{dM dx_F} \Big|_{x_F=0}$ using the 1-, 2-loop and resummed hard parts in fig. 8. The resummed curve has an excellent fit, while both finite order curves underestimate the data. Again, as in the NA3(1980) \bar{p} on Pt case, the error bars are so large that all three curves are within them.

4.5 The E605 Experiment

In this Fermilab experiment [19], a proton beam was incident on a copper (Cu) target at $\sqrt{s} = 38.8$ GeV. We show in figs. 9a and 9b the data points with the 1-loop, 2-loop and resummed predictions for $s \frac{d^2\sigma}{d\sqrt{\tau} dy} \Big|_{y=0}$ using the CTEQ2D and MRSD- distributions, respectively.

E605 data together with a 1-loop hard part as a theoretical input, were used for the CTEQ global fit, so, as expected, the 1-loop curve in fig. 9 gives an excellent fit to the data over the whole range of τ . The resummed cross section is about 18 to 14% bigger than the data, but within experimental errors, the difference decreasing on average as τ increases.

In fig. 9b, the 1-loop curve also has the best fit to the data but with some overestimate. The 2-loop and resummed curves overestimate the data, and are about 10% bigger than their CTEQ2D counterparts in fig. 9a.

4.6 The E772 Experiment

This recent Fermilab experiment [20] focused on interactions of a proton beam with various targets, to obtain, among other things, the nuclear dependence of the resulting spectrum. Here we will look at p - ^2H cross sections at $\sqrt{s} = 38.8$ GeV and $x_F > 0$.

In fig. 10, we plot the mass distribution $M_{\mu\mu}^3 \frac{d\sigma}{dM_{\mu\mu}} \Big|_{x_F>0}$ using the CTEQ2D parton distributions. In the low mass region ($.1 < \sqrt{\tau} < .24$), the resummed curve has the best fit to the data. In the high mass region ($.1 < \sqrt{\tau} < .24$), the 1-loop curve has the best fit. However, the resummed and 2-loop curves are no more than 16% bigger than the 1-loop curve, and within experimental errors.

We show in fig. 11 the distribution $M_{\mu\mu}^3 \frac{d^2\sigma}{dM_{\mu\mu} dx_F} \Big|_{x_F=0}$ using CTEQ2D parton distributions. In the high mass region, all three curves pass through almost all of the error bars. The resummed and 2-loop curves, which in this case are almost identical, have the best fit. In the low mass region, the 2-loop cross section gives a good fit, with some slight underestimate. The resummed curve overshoots the data by 18% or less.

4.7 K -factors

We have also calculated a set of K -factors for the kinematics of various experiments using eqs. (12), (17), (21) and (19). Note that the denominator is simply the Leading Logarithm Approximation (LLA) cross section. For figs. 12 and 14, the K factors were calculated over the full rapidity range, while for fig. 13, the K 's were only calculated over positive rapidity.

These quantities express the size of the resummed radiative corrections relative to lowest order. They turn out to be relatively insensitive to the parton sets used, and allow us to compare the importance of corrections for the various experiments.

In fig. 12, we plot K_1 , K_2 and the resummed K factor, using parameters from the E537 experiment described above and the CTEQ2D parton distributions. K_i is the i -th loop K -factor obtained using eq. (21). To better illustrate the different contributions to K , we show two other curves in the same plot: the dot-dashed and dotted curves are resummed curves but with $A(\alpha)$ (eq. (58)) replaced by $A_1(\alpha)$ (eq. (48)) and 1, respectively.

We see that, in the mass range covered by the plot, most of the resummed K comes from the $A(\alpha)$ term, as the plus distributions in this case account from only a few percent to about 26% of the total K . This agrees with an earlier assessment given in the cross section discussions. Comparing the solid and dot-dashed curves, one also observes that the next-to-leading terms in the exponent of $A(\alpha)$ yield from 3 to 7% contribution to the resummed cross sections.

In fig. 13, we present our theoretical resummed K -factor, along with K_1 and K_2 for the NA3 (1985) experiment, using two different parton sets: CTEQ2D and MRSD-. We notice that the resulting curves are in very good agreement with one another.

In fig. 14, we present the K -factors, using the CTEQ2D parton distributions for the E772 experiment. What is important to note here is that as one goes to large mass values, the difference between the resummed and the 2-loop K -factor decreases to about a few percent. Moreover, whereas K_1 and K_2 are noticeably increasing in this region and beyond, K is relatively flat or very smoothly decreasing. This highlights the “well-behaved” nature of principal value resummation, for it is precisely in this region where the logarithms in perturbative calculations are large.

4.8 Theoretical Uncertainty

In this section, we quantify the theoretical uncertainty in our resummed calculations, as well as the goodness-of-fit of both resummed and finite-order cross sections. For purposes of discussion, we focus on data from the E605 and E537 experiments.

We compare in fig. 15 the resummed cross sections calculated using CTEQ2D and MRSD- parton distributions with data from E605. We see that the 2 curves are within 10% of each other. There is also an estimated uncertainty of about 7% due to contributions of non-singular terms that were not included in the resummed hard part (see discussion in section 5). Thus, we consider a good estimate of the theoretical uncertainty in the resummed predictions to be 17%.

In table 1, we present the χ^2 per degree of freedom of the calculated cross sections relative to data from E605. As expected, the 1-loop cross sections calculated with global parton sets have the best χ^2 values. However, one also notes that the χ^2 's of the resummed cross sections are not that large compared with the best values. ⁷

⁷In [21], we discuss the possibility that this difference is related to nonperturbative effects.

TABLE 1

χ^2 per degree of freedom (E605)			
Parton set	Resummed	1-loop	2-loop
CTEQ2D	5.0	1.3	2.1
MRSD-	11.6	2.6	5.9

Similarly, we present in table 2 the analogous χ^2 values for the experiment E537, using the data points shown in our fig. 8. In this case, the resummed cross sections have the best χ^2 values, while the finite-order cross sections have χ^2 's not more than 1. This supports our earlier claim that for antiprotons on fixed targets the resummed cross section has the best fit.

TABLE 2

χ^2 per degree of freedom (E537)			
Parton set	Resummed	1-loop	2-loop
CTEQ2D	0.05	0.38	0.84
MRSD-	0.14	0.46	0.93

5 Discussion and Conclusions

In this paper, we have used a previously calculated hard part [2] for dilepton production, which resums large threshold corrections to all orders in pQCD via the method of principal value resummation [3], to calculate resummed DY distributions. We have also derived the coefficient function $A(\alpha)$, which involves the resummation of large, z -independent Sudakov terms, to next-to-leading order. We then made comparisons of several distributions with data from fixed-target experiments. In as much as the available data cover only the positive rapidity region, we used the approximation of [12] in our calculations. All calculations have been made in the DIS scheme. To be entirely consistent, one should use parton distributions resulting purely from fits to Deep Inelastic Scattering data. Existing DIS fits (like DFLM [22] and EHLQ [23]), however, had been constructed from relatively old data. On the other hand, the global fits (like CTEQ2D and MRSD-) that we have used, typically use only 1-loop hard parts for input in hadron-hadron scattering, for example when Drell-Yan data is included, but include the most recent DIS data. If higher order corrections are important, their effects will be included in the globally fitted distributions, and using them in a resummed calculation would involve some double-counting and thus lead to overestimates.

We now summarize our results in the light of these issues. For all fixed-target experiments we have examined, the resummed cross sections exhibit good to excellent agreement with the data. For antiprotons on fixed targets, we find in general that the resummed predictions agree better than the finite-order ones. For proton beams the finite-order predictions agree better in most cases, but in those cases the resummed ones are above the data by no more than 10–23% and even then, all predictions are within experimental errors. From the above, we can conclude that principal value resummation has successfully “tamed” the divergences in perturbation theory associated with the resummation of plus-distributions. We find that even if large corrections exist at the 1- and 2-loop order, principal value resummation yields cross sections that are finite and well-behaved. In addition, the quantitative structure of

the large threshold corrections in principal value resummation correctly accounts for the observed data.

It is important here to summarize what these results represent concerning our knowledge of perturbative QCD. Our resummed cross sections were calculated including all the radiation phase space down to threshold. This includes the perturbative regime, which provides the bulk of the effect, and the non-perturbative regime which we treat via the principal value resummation model.

The fact that, using global parton sets, the resummed cross section slightly overshoots most proton beam data, needs to be disentangled:

It would be useful if a parton set fitted only to the most recent DIS data becomes available, so that one could repeat our resummed calculations with this set. If, however, the antiquark fits are so “robust” that the resulting cross sections do not change significantly then the following issues, which could possibly explain the overestimate, need to be confronted. First, the cross section could be sensitive to higher twist. The physical higher-twist would be slightly different than in principal value resummation, and should be parametrized more generally. This issue is studied in more detail in [21].

Secondly, the factor $A(\alpha)$ accounts for a large part of the resummed cross section. It is important to note that only the exponentiation of Sudakov terms in $A(\alpha)$ is fully understood at this moment. Since the exponent of eq. (58) contains some finite non-Sudakov terms as well, following [24], a better understanding of the resummation of these terms in this function is also needed to eliminate some of the theoretical uncertainty. It might be that inclusion of such terms might make $A(\alpha)$ smaller, so that the resummed cross section is also reduced.

Another issue is the size of the non-singular terms in the hard part at higher orders. For the case of the 2-loop order, the size of the contributions of these non-singular terms has been studied. From [11], we note that in the kinematic region we have considered, the non-singular terms in the 2-loop hard part yield from 5 to 10% negative contributions to the cross section. In the resummed case, those terms will lead up to a 7% negative contribution.⁸ If such “finite” terms continue to be sizeable at still higher orders, however, they might further reduce the effects of resummation, which might explain why 1- or 2-loop cross sections that use global parton sets can describe the data quite well.

All of these issues are correlated in the differences of our predictions using different parton sets, and the 2-loop reduction of the non-singular terms. Our uncertainty estimate of 17% is in fact a conservative measure of these factors and clearing-up these issues corresponds to narrowing down this theoretical uncertainty.

In future work we hope to extend these calculations in the context of collider energies, both for the Drell-Yan continuum and for vector boson production. Among the most interesting other reactions sharing many common features with dilepton production, and where principal value resummation has been advantageously applied, is top-quark production [25].

ACKNOWLEDGMENTS

We thank George Sterman for many valuable suggestions, and Ed Berger, Eric Laenen, Jeff Owens, Jack Smith and Wu-Ki Tung for many helpful discussions. This work was supported in part by the U.S. Department of Energy, Division of High Energy Physics,

⁸Note that we did not include the 2-loop non-singular contributions in our central value predictions, but we did so in our uncertainty estimate.

contract W-31-109-ENG-38, and by the National Science Foundation, grant PHY 9309888.

APPENDIX A Some Notes on the Numerical Calculations

The explicit expression used to calculate the resummed cross section in this paper is

$$\frac{d\sigma}{dQ^2} = \sigma_B \sum_f e_f^2 \int_\tau^1 dz A(\alpha) [1 + \mathcal{H}(z, \alpha)] \frac{d}{dz} \left(\frac{\mathcal{F}_{f\bar{f}}(\tau/z)}{z} \right), \quad (61)$$

where σ_B is given by eq. (7), $A(\alpha)$ by eq. (58), $\mathcal{H}(z, \alpha)$ by eq. (18) and the parton luminosity by eq. (5). The factor involving the luminosity can be expressed as an integral over the rapidity y [4]:

$$\frac{d}{dz} \left(\frac{\mathcal{F}_{f\bar{f}}(\tau/z)}{z} \right) = -\frac{1}{2z^2} \int_{y^-}^{y^+} dy \left(2 + x_1 \frac{d}{dx_1} + x_2 \frac{d}{dx_2} \right) F_{f/h_1}(x_1, Q^2) F_{\bar{f}/h_2}(x_2, Q^2), \quad (62)$$

where $x_1 = \sqrt{\frac{\tau}{z}} e^y$, $x_2 = \sqrt{\frac{\tau}{z}} e^{-y}$ and $y^\pm = \pm \frac{1}{2} \log(\frac{z}{\tau})$.

Note that eq. (61) may now be re-written as

$$\begin{aligned} \frac{d\sigma}{dQ^2} &= A(\alpha) \frac{d\sigma_0}{dQ^2} + A(\alpha) \sigma_B \sum_f e_f^2 \int_\tau^1 dz \mathcal{H}(z, \alpha) \left(-\frac{1}{2z^2} \right) \int_{y^-}^{y^+} dy \left(2 + x_1 \frac{d}{dx_1} + x_2 \frac{d}{dx_2} \right) \\ &\quad \times F_{f/h_1}(x_1, Q) F_{\bar{f}/h_2}(x_2, Q), \end{aligned} \quad (63)$$

with $\frac{d\sigma_0}{dQ^2}$ as in eq. (11). With the integral definition of $\mathcal{H}(z, \alpha)$, eq. (18), one has to perform at least four integrations to compute $d\sigma/dQ^2$ for one value of Q .⁹ Straightforward implementation of eq. (61) is thus very time-consuming from a numerical point of view.

In order to shorten significantly the processing time requirements, an intermediate step was performed: the quantity $\mathcal{H}(z, \alpha)$ was first interpolated over a range of z and α values. The interpolation is essentially a two parameter (z, α) fit to a set of $\mathcal{H}(z, \alpha)$ values calculated over the box contour for particular values of z and α . But because E (and thus P_1)¹⁰ depends on parameters which in turn depend on n_f , there is an implicit dependence of $\mathcal{H}(z, \alpha)$ on n_f . Furthermore, note that one can have a leading or next-to-leading $\mathcal{H}(z, \alpha)$ depending on whether $E = E_L$ or $E = E_L + E_{NL}$ is used. For all the fixed target cross section calculations, $n_f = 4$ and $E = E_L + E_{NL}$ were used.

Armed with the interpolating function, the calculation of eq. (63) becomes a little simpler (for now, only a 2-fold integral is involved) and more importantly, a lot faster from a numerical point of view.

The interpolating function, which we will now denote by $\mathcal{H}_I(z, \alpha)$,¹¹ is valid for $.01 < z < 1 - 10^{-6}$ and $4.756 \times 10^{-2} < \alpha < 7.197 \times 10^{-2}$. The choice of the boundaries for z is essentially machine-dependent: outside this range in z , the program ran into round-off errors. Hence, when $\mathcal{H}_I(z, \alpha)$ is used in eq. (63), the upper z -limit is taken to be $1 - 10^{-6}$. As mentioned in our previous paper [2], for fixed α , the exact $\mathcal{H}(z, \alpha)$ is bounded, reaching a certain limiting value before $z \rightarrow 1 - 10^{-6}$. The contribution from the region $z > 1 - 10^{-6}$ is thus expected to be very small and may be neglected.

⁹Aside from the z, z' and y integrals, further integrations are required to calculate E and P_1 .

¹⁰In calculating the set of $\mathcal{H}(z, \alpha)$ values, E was calculated over a box contour [3] while P_1 was calculated numerically: $P_1(z) = (1-z) \frac{E(z+h) - E(z-h)}{2h}$ for some small number h .

¹¹The interpolations were obtained using the B spline routines in the Fortran 77 IMSL package.

For the finite order calculations, instead of eq. (61), (62), we use

$$\frac{d\sigma^i}{dQ^2} = \sigma_B \sum_{j=0}^i \sum_{a,b} C_{ab}^V \int_{\tau}^1 dz \left[\int_z^1 dz' \alpha^j \omega_{ab}^{(j)}(z', \alpha) \right] \left(-\frac{1}{2z^2} \right) \int_{y^-}^{y^+} dy \left(2 + x_1 \frac{d}{dx_1} + x_2 \frac{d}{dx_2} \right) \times F_{a/h_1}(x_1, Q) F_{b/h_2}(x_2, Q), \quad (64)$$

with C_{ab}^V given in section 2.1 and $\omega_{ab}^i(z', \alpha)$ given by eqs. (22)-(25). No interpolations were necessary for the finite-order hard-parts.

For the exact calculation of $\frac{d\sigma_{q\bar{q}}^{(1)}}{dQ^2 dy} \Big|_{y=0}$, we used the results given in [13]. The explicit expression for the $q\bar{q}$ channel is

$$\frac{d\sigma_{q\bar{q}}^{(1)}}{dQ^2 dy} \Big|_{y=0} = \frac{16\pi \alpha_e^2 \alpha}{27 Q^2 s} \sum_f e_f^2 \sum_{j=1}^5 T_{f\bar{f}}^j, \quad (65)$$

with

$$\begin{aligned} T_{f\bar{f}}^1 &= \frac{1}{2} \left[1 + \frac{5}{3}\pi^2 - \frac{3}{2} \ln \frac{x_1 x_2}{(1-x_1)(1-x_2)} + 2 \ln \frac{x_1}{(1-x_1)} \ln \frac{x_2}{(1-x_2)} \right] P_{f\bar{f}}(x_1, x_2, Q), \\ T_{f\bar{f}}^2 &= \frac{1}{2} \int_{x_1}^1 dt_1 \left(\frac{t_1^2 + x_1^2}{t_1^2 (t_1 - x_1)_+} \ln \frac{2x_1(1-x_2)}{x_2(t_1+x_1)} + \frac{3}{2} \frac{1}{(t_1-x_1)_+} - \frac{2}{t_1} - \frac{3x_1}{t_1^2} \right) P_{f\bar{f}}(t_1, x_2, Q), \\ T_{f\bar{f}}^3 &= \frac{1}{2} \int_{x_2}^1 dt_2 \left(\frac{t_2^2 + x_2^2}{t_2^2 (t_2 - x_2)_+} \ln \frac{2x_2(1-x_1)}{x_1(t_2+x_2)} + \frac{3}{2} \frac{1}{(t_2-x_2)_+} - \frac{2}{t_2} - \frac{3x_2}{t_2^2} \right) P_{f\bar{f}}(x_1, t_2, Q), \\ T_{f\bar{f}}^4 &= \int_{x_1}^1 dt_1 \int_{x_2}^1 dt_2 \frac{G^A(t_1, t_2)}{[(t_1-x_1)(t_2-x_2)]_+} P_{f\bar{f}}(t_1, t_2, Q), \\ T_{f\bar{f}}^5 &= \int_{x_1}^1 dt_1 \int_{x_2}^1 dt_2 \frac{-2\tau(\tau+t_1 t_2)}{t_1 t_2 (t_1 x_2 + t_2 x_1)^2} P_{f\bar{f}}(t_1, t_2, Q), \end{aligned} \quad (66)$$

where $x_1 = x_2 = \sqrt{\tau}$, $P_{f\bar{f}}(t_1, t_2, Q) = F_{f/h_1}(t_1, Q^2) F_{\bar{f}/h_2}(t_2, Q^2)$ and

$$G^A(t_1, t_2) = \frac{(\tau + t_1 t_2)(\tau^2 + (t_1 t_2)^2)}{(t_1 t_2)^2 (t_1 + x_1)(t_2 + x_2)}. \quad (67)$$

The sum in eq. (65) extends over all active quark and antiquark flavors. Eqs. (65) and (66) were obtained using eqs. (2.1), (2.3), (2.6)-(2.8) of [13]. The $+$ distributions are evaluated using the prescription given by their eqs. (2.9) and (2.10).

Similarly, for the quark-gluon channel, we used eqs. (2.13)-(2.17) of [13] to obtain

$$\frac{d\sigma_{qg}^{(1)}}{dQ^2 dy} \Big|_{y=0} = \frac{2\pi \alpha_e^2 \alpha}{9 Q^2 s} \sum_f e_f^2 \sum_{j=1}^6 U_{gf}^j, \quad (68)$$

with

$$\begin{aligned} U_{gf}^1 &= \int_{x_1}^1 dt_1 \left(\frac{x_1^2 + (t_1 - x_1)^2}{2t_1^3} \ln \frac{2x_1(1-x_2)}{x_2(t_1+x_1)} + \frac{1}{2t_1} - \frac{3x_1(t_1-x_1)}{t_1^3} \right) P_{gf}^C(t_1, x_2, Q), \\ U_{gf}^2 &= \int_{x_1}^1 dt_1 \int_{x_2}^1 dt_2 \frac{G^C(t_1, t_2)}{(t_2-x_2)_+} P_{gf}^C(t_1, t_2, Q), \\ U_{gf}^3 &= \int_{x_1}^1 dt_1 \int_{x_2}^1 dt_2 H^C(t_1, t_2) P_{gf}^C(t_1, t_2, Q), \\ U_{gf}^4 &= \int_{x_2}^1 dt_2 \left(\frac{x_2^2 + (t_2 - x_2)^2}{2t_2^3} \ln \frac{2x_2(1-x_1)}{x_1(t_2+x_2)} + \frac{1}{2t_2} - \frac{3x_2(t_2-x_2)}{t_2^3} \right) P_{gf}^C(t_2, x_1, Q), \\ U_{gf}^5 &= \int_{x_2}^1 dt_2 \int_{x_1}^1 dt_1 \frac{G^C(t_2, t_1)}{(t_1-x_1)_+} P_{gf}^C(t_2, t_1, Q), \\ U_{gf}^6 &= \int_{x_2}^1 dt_2 \int_{x_1}^1 dt_1 H^C(t_2, t_1) P_{gf}^C(t_2, t_1, Q), \end{aligned} \quad (69)$$

where

$$\begin{aligned}
G^C(t_1, t_2) &= \frac{x_2(\tau+t_1t_2)(\tau^2+(\tau-t_1t_2)^2)}{t_1^3t_2^2(t_1x_2+t_2x_1)(t_2+x_2)}, \\
H^C(t_1, t_2) &= \frac{\tau(\tau+t_1t_2)(t_1t_2^2x_1+\tau(t_1x_2+2t_2x_1))}{(t_1t_2)^2(t_1x_2+t_2x_1)^3}, \\
P_{gf}^C(t_1, t_2, Q) &= F_{g/h_1}(t_1, Q^2)F_{f/h_2}(t_2, Q^2), \\
P_{gf}^C(t_2, t_1, Q) &= F_{g/h_2}(t_2, Q^2)F_{f/h_1}(t_1, Q^2).
\end{aligned} \tag{70}$$

For the exact calculation of $\left. \frac{d\sigma_{q\bar{q}}^{(1)}}{dQ^2} \right|_{y>0}$, we used

$$\left. \frac{d\sigma_{q\bar{q}}^{(1)}}{dQ^2} \right|_{y>0} = \frac{16\pi}{27} \frac{\alpha_e^2 \alpha}{Q^2 s} \sum_f e_f^2 \sum_{j=1}^5 S_{f\bar{f}}^j, \tag{71}$$

with

$$\begin{aligned}
S_{f\bar{f}}^1 &= \frac{1}{2} \int_{\sqrt{\tau}}^1 \frac{dx_1}{x_1} \left(1 + \frac{5}{3}\pi^2 - \frac{3}{2} \ln \frac{\tau}{(1-x_1)(1-\tau/x_1)} + 2 \ln \frac{x_1}{(1-x_1)} \ln \frac{\tau}{(x_1-\tau)} \right) P_{f\bar{f}}(x_1, \tau/x_1, Q), \\
S_{f\bar{f}}^2 &= \frac{1}{2} \int_{\sqrt{\tau}}^1 \frac{dx_1}{x_1} \int_{x_1}^1 dt_1 \left(\frac{t_1^2+x_1^2}{t_1^2(t_1-x_1)_+} \ln \frac{2x_1(x_1-\tau)}{\tau(t_1+x_1)} + \frac{3}{2} \frac{1}{(t_1-x_1)_+} - \frac{2}{t_1} - \frac{3x_1}{t_1^2} \right) P_{f\bar{f}}(t_1, \tau/x_1, Q), \\
S_{f\bar{f}}^3 &= \frac{1}{2} \int_{\sqrt{\tau}}^1 \frac{dx_2}{x_2} \int_{x_2}^1 dt_2 \left(\frac{t_2^2+x_2^2}{t_2^2(t_2-x_2)_+} \ln \frac{2x_2(x_2-\tau)}{\tau(t_2+x_2)} + \frac{3}{2} \frac{1}{(t_2-x_2)_+} - \frac{2}{t_2} - \frac{3x_2}{t_2^2} \right) P_{f\bar{f}}(\tau/x_2, t_2, Q), \\
S_{f\bar{f}}^4 &= \int_{\sqrt{\tau}}^1 \frac{dx_1}{x_1} \int_{x_1}^1 dt_1 \int_{\tau/x_1}^1 dt_2 \frac{G^A(t_1, t_2)}{[(t_1-x_1)(t_2-\tau/x_1)]_+} P_{f\bar{f}}(t_1, t_2, Q), \\
S_{f\bar{f}}^5 &= \int_{\sqrt{\tau}}^1 \frac{dx_1}{x_1} \int_{x_1}^1 dt_1 \int_{\tau/x_1}^1 dt_2 \frac{-2\tau(\tau+t_1t_2)}{t_1t_2(t_1\tau/x_1+t_2x_1)^2} P_{f\bar{f}}(t_1, t_2, Q).
\end{aligned} \tag{72}$$

Eqs. (71) and (72) were obtained using eqs. (2.6) and (C.1) of [13]. Note that the integration limits for x_1, x_2 follow from the requirement that $y > 0$ or equivalently, $x_F = x_1 - x_2 > 0$.

In a similar way, starting from their eqs. (2.17) and (C.1), the following formula is obtained for the quark-gluon channel:

$$\left. \frac{d\sigma_{qg}^{(1)}}{dQ^2} \right|_{y>0} = \frac{2\pi}{9} \frac{\alpha_e^2 \alpha}{Q^2 s} \sum_f e_f^2 \sum_{j=1}^6 V_{gf}^j, \tag{73}$$

with

$$\begin{aligned}
V_{gf}^1 &= \int_{\sqrt{\tau}}^1 \frac{dx_1}{x_1} \int_{x_1}^1 dt_1 \left(\frac{x_1^2+(t_1-x_1)^2}{2t_1^3} \ln \frac{2x_1(x_1-\tau)}{\tau(t_1+x_1)} + \frac{1}{2t_1} - \frac{3x_1(t_1-x_1)}{t_1^3} \right) P_{gf}^C(t_1, \tau/x_1, Q), \\
V_{gf}^2 &= \int_{\sqrt{\tau}}^1 \frac{dx_2}{x_2} \int_{\tau/x_2}^1 dt_1 \int_{x_2}^1 dt_2 \frac{G^C(t_1, t_2)}{(t_2-x_2)_+} P_{gf}^C(t_1, t_2, Q), \\
V_{gf}^3 &= \int_{\sqrt{\tau}}^1 \frac{dx_1}{x_1} \int_{x_1}^1 dt_1 \int_{\tau/x_1}^1 dt_2 H^C(t_1, t_2) P_{gf}^C(t_1, t_2, Q), \\
V_{gf}^4 &= \int_{\sqrt{\tau}}^1 \frac{dx_2}{x_2} \int_{x_2}^1 dt_2 \left(\frac{x_2^2+(t_2-x_2)^2}{2t_2^3} \ln \frac{2x_2(x_2-\tau)}{\tau(t_2+x_2)} + \frac{1}{2t_2} - \frac{3x_2(t_2-x_2)}{t_2^3} \right) P_{gf}^C(t_2, \tau/x_2, Q), \\
V_{gf}^5 &= \int_{\sqrt{\tau}}^1 \frac{dx_1}{x_1} \int_{\tau/x_1}^1 dt_2 \int_{x_1}^1 dt_1 \frac{G^C(t_2, t_1)}{(t_1-x_1)_+} P_{gf}^C(t_2, t_1, Q), \\
V_{gf}^6 &= \int_{\sqrt{\tau}}^1 \frac{dx_1}{x_1} \int_{\tau/x_1}^1 dt_2 \int_{x_1}^1 dt_1 H^C(t_2, t_1) P_{gf}^C(t_2, t_1, Q).
\end{aligned} \tag{74}$$

All of the various parton distributions used were taken from the CERN PDFLIB package.

FIGURE CAPTIONS

Figure 1. Exact and approximate $s \frac{d^2\sigma}{d\sqrt{\tau}dy} \Big|_{y=0}$ to $\mathcal{O}(\alpha)$.

Solid=exact calculation using results of Kubar et al in [13];
Dotted=calculated using Laenen-Sterman approximation.

Figure 2. Exact and approximate $M_{\mu\mu}^3 \frac{d\sigma}{dM_{\mu\mu}} \Big|_{x_F>0}$ to $\mathcal{O}(\alpha)$.

Solid=exact calculation using results of Kubar et al in [13];
Dotted=calculated using Laenen-Sterman approximation.

Figure 3. Different forms of $A(\alpha)$.

Solid= $A(\alpha)$; Dashed= $A_2(\alpha)$; Dotted= $A_1(\alpha)$.

Figure 4. NA3(1980): $M_{\mu\mu}^3 \frac{d\sigma}{dM_{\mu\mu}} \Big|_{x_F>0}$.

(a) CTEQ2D. Solid=resummed; Long Dashed=2-loop; Short Dashed=1-loop.
(b) Same as (a) but for MRS D-.

Figure 5. Contributions to $M_{\mu\mu}^3 \frac{d\sigma}{dM_{\mu\mu}} \Big|_{x_F>0}$.

Solid=total resummed cross section; Dashed=resummed but with $A(\alpha)$ replaced by 1;
Dotted=Born cross section.

Figure 6. NA3(1985): $M_{\mu\mu}^3 \frac{d\sigma}{dM_{\mu\mu}} \Big|_{x_F>0}$ using CTEQ2D partons.

Solid=resummed; Long Dashed=2-loop; Short Dashed=1-loop.

Figure 7. E537: $M_{\mu\mu}^3 \frac{d\sigma}{dM_{\mu\mu}} \Big|_{x_F>0}$ using CTEQ2D partons.

Solid=resummed; Long Dashed=2-loop; Short Dashed=1-loop.

Figure 8. E537: $M^3 \frac{d^2\sigma}{dMdx_F} \Big|_{x_F=0}$ using CTEQ2D partons.

Solid=resummed; Long Dashed=2-loop; Short Dashed=1-loop.

Figure 9. E605: $s \frac{d^2\sigma}{d\sqrt{\tau}dy} \Big|_{y=0}$.

Solid=resummed; Long Dashed=2-loop; Short Dashed=1-loop.

(a) CTEQ2D.
(b) MRSD-.

Figure 10. E772: $M_{\mu\mu}^3 \frac{d\sigma}{dM_{\mu\mu}} \Big|_{x_F>0}$ using CTEQ2D partons.

Solid=resummed; Long Dashed=2-loop; Short Dashed=1-loop.

Figure 11. E772: $M^3 \frac{d^2\sigma}{dM dx_F} \Big|_{x_F=0}$ using CTEQ2D partons.
 Solid=resummed; Long Dashed=2-loop; Short Dashed=1-loop.

Figure 12. K factors for E537 \bar{p} -W using CTEQ2D.
 Solid=resummed; Long Dashed=2-loop; Short Dashed=1-loop;
 Dot-Dashed=resummed with $A(\alpha)$ replaced by $A_1(\alpha)$;
 Dotted=resummed with $A(\alpha)$ replaced by 1.

Figure 13. NA3(1985) theoretical K -factors for different parton sets.
 Dashed (descending order): Same as above using MRSD-;
 Dotted (descending order): Same as above using CTEQ2D.

Figure 14. K -factors for E772 p - ^2H using CTEQ2D.
 Solid=resummed; Long Dashed=2-loop; Short Dashed=1-loop.

Figure 15. Resummed curves for E605 using global fits.
 Upper solid curve=MRSD-; Lower solid curve=CTEQ2D.

References

- [1] G. Altarelli, R.K. Ellis and G. Martinelli, Nucl. Phys. B157 (1979) 461;
 B. Humpert and W.L. van Neerven, Phys. Lett. B84 (1979) 327;
 J. Kubar-Andre and F.E. Paige, Phys. Rev. D19 (1979) 221;
 K. Harada, T. Kaneko and N. Sakai, Nucl. Phys. B155 (1979) 169; B165 (1980) 545 (E);
 T. Matsuura and W. L. van Neerven, Z. Phys. C38 (1988) 623;
 T. Matsuura, S.C. van der Marck and W.L. van Neerven, Phys. Lett. B211 (1988) 171.
- [2] L. Alvero and H. Contopanagos, Nucl. Phys. B436 (1995) 184.
- [3] H. Contopanagos and G. Sterman, Nucl. Phys. B419 (1994) 77.
- [4] D. Appell, P. Mackenzie and G. Sterman, Nucl. Phys. B309 (1988) 259.
- [5] T. Matsuura, S.C. van der Marck and W.L. van Neerven, Nucl. Phys. B319 (1989) 570.
- [6] L. Magnea and G. Sterman, Phys. Rev. D42 (1990) 4222.
- [7] R. Hamberg, W.L. van Neerven and T. Matsuura, Nucl. Phys. B359 (1991) 343.
- [8] CTEQ collaboration (G. Sterman, editor) *Handbook of perturbative QCD*, version 1.0 (April 1993).
- [9] H. Contopanagos and G. Sterman, Nucl. Phys. B400 (1993) 211.
- [10] W.L. van Neerven and E.B. Zijlstra, Nucl. Phys. B382 (1992) 11.
- [11] P.J. Rijken and W.L. van Neerven, Phys. Rev. D51 (1995) 44.

- [12] E. Laenen and G. Sterman, *The Fermilab Meeting*, DPF'92, Vol. 2, 987 (C. Albright et al., editors).
- [13] J. Kubar, M. Le Bellac, J.L. Meunier and G. Plaut, Nucl. Phys. B175 (1980) 251.
- [14] CTEQ Collaboration, unpublished; H.L. Lai et al., MSU-HEP-41024/CTEQ-404 (October 1994).
- [15] A.D. Martin, W.J. Stirling and R.G. Roberts, Phys. Rev. D47 (1993) 867; Phys. Lett. 306B (1993) 145.
- [16] J. Badier et al., Phys. Lett. B96 (1980) 422.
- [17] J. Badier et al., Z. Phys. C26 (1985) 489.
- [18] E. Anassontzis et al., Phys. Rev. D38 (1988) 1377.
- [19] G. Moreno et al., Phys. Rev. D43 (1991) 2815.
- [20] P.L. McGaughey et al. (E772 Collaboration), Phys. Rev. D50 (1994) 3038.
- [21] L. Alvero, ITP-SB-94-67 (December 1994), hep-ph 9412335.
- [22] M. Diemoz, F. Ferroni, E. Longo and G. Martinelli, Z. Phys. C39 (1988) 21.
- [23] E. Eichten, I. Hinchliffe, K. Lane and C. Quigg, Rev. Mod. Phys. 56 (1984) 579.
- [24] G. Sterman, Nucl. Phys. B281 (1987) 310;
S. Catani and L. Trentadue, Nucl. Phys. B327 (1989) 323; B353 (1991) 183.
- [25] E. Berger and H. Contopanagos, ANL-HEP-PR-95-31 (July 1995).

This figure "fig1-1.png" is available in "png" format from:

<http://arxiv.org/ps/hep-ph/9411294v2>

p Cu (38.8 GeV)

CTEQ2D ($\Lambda_4=0.235\text{GeV}$)

E605

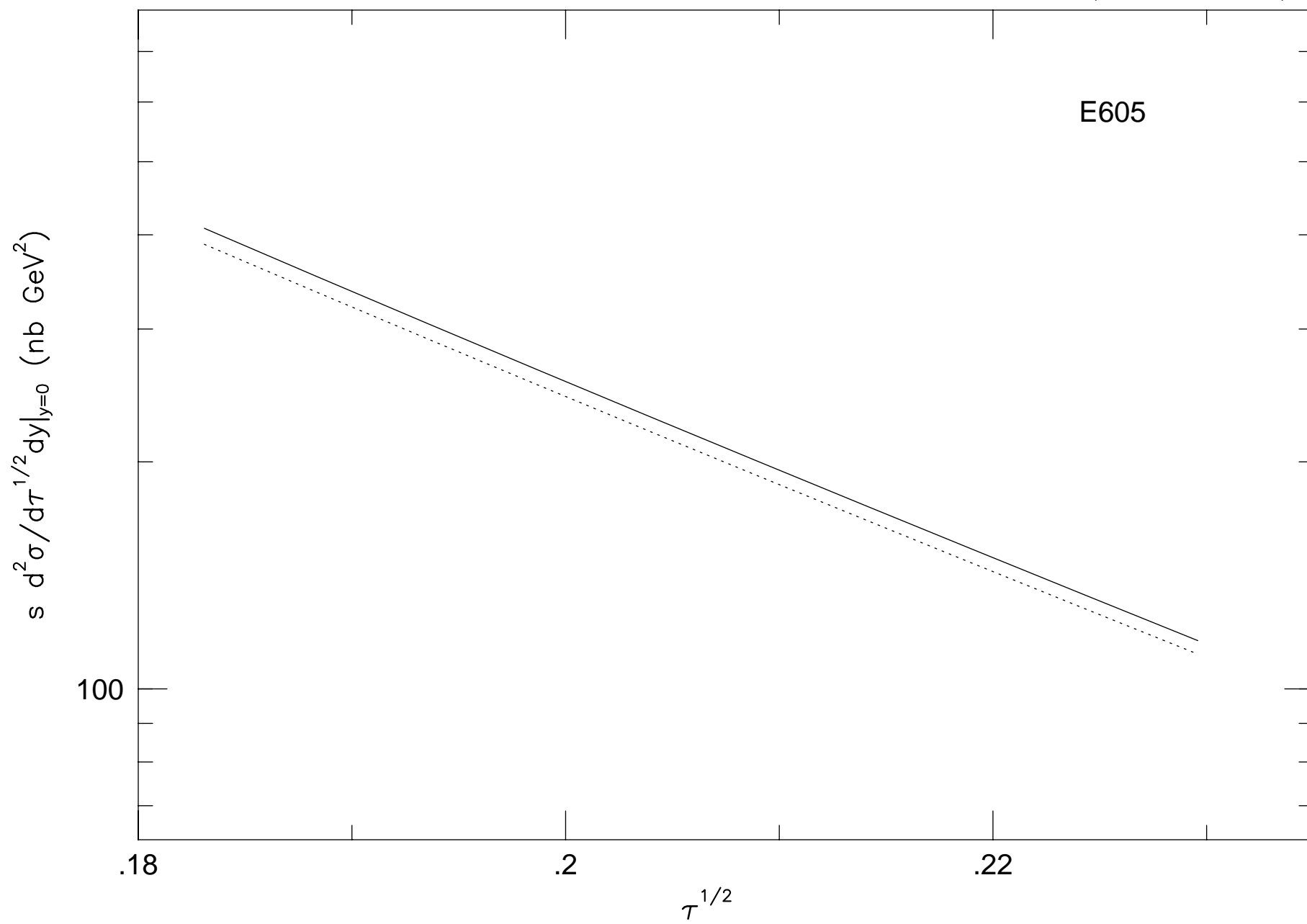


Fig. 1

This figure "fig2-1.png" is available in "png" format from:

<http://arxiv.org/ps/hep-ph/9411294v2>

This figure "fig3-1.png" is available in "png" format from:

<http://arxiv.org/ps/hep-ph/9411294v2>

This figure "fig4-1.png" is available in "png" format from:

<http://arxiv.org/ps/hep-ph/9411294v2>

This figure "fig1-2.png" is available in "png" format from:

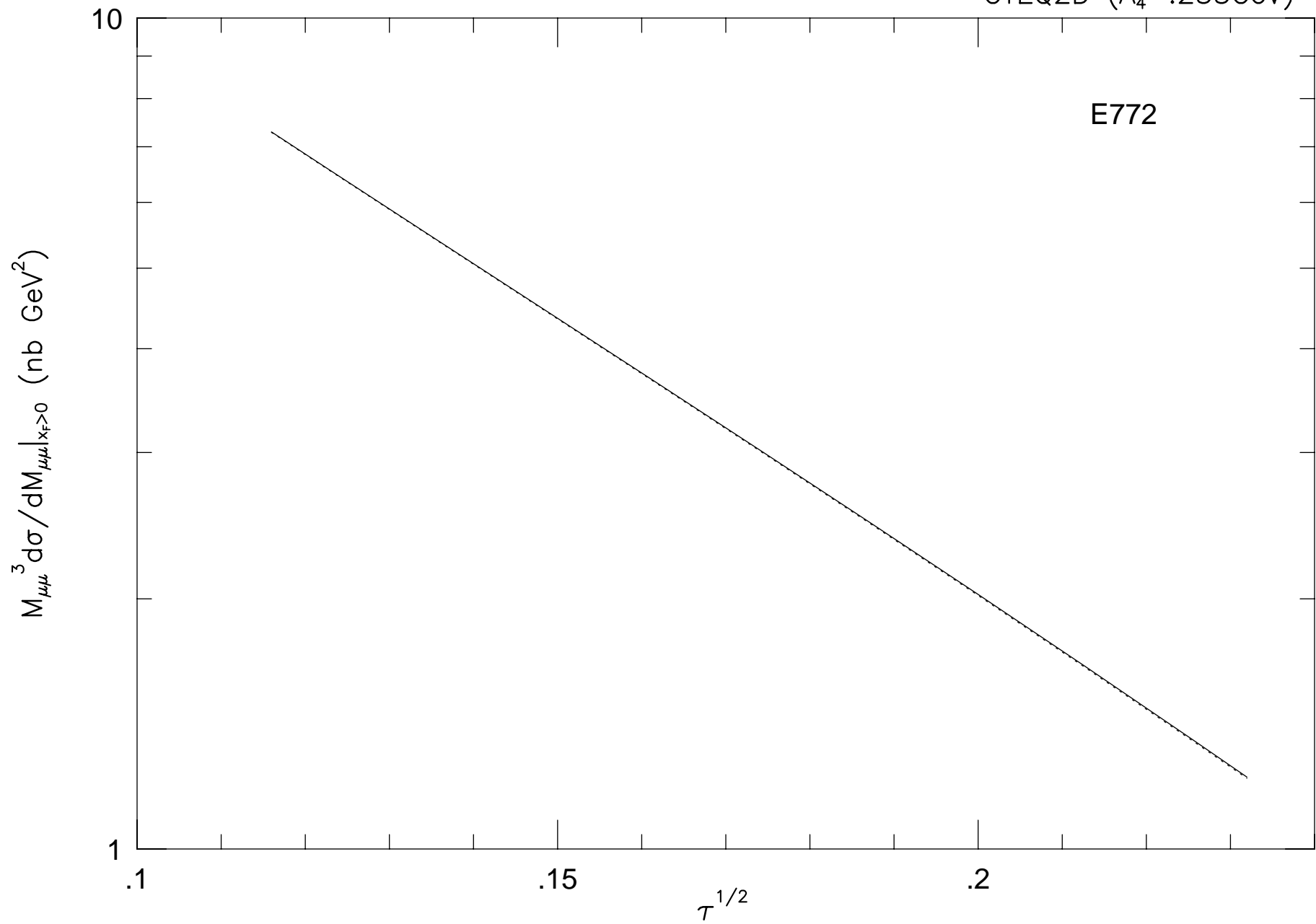
<http://arxiv.org/ps/hep-ph/9411294v2>

This figure "fig2-2.png" is available in "png" format from:

<http://arxiv.org/ps/hep-ph/9411294v2>

p ²H (38.8 GeV)

CTEQ2D ($\Lambda_4=.235\text{GeV}$)



E772

Fig. 2

This figure "fig3-2.png" is available in "png" format from:

<http://arxiv.org/ps/hep-ph/9411294v2>

This figure "fig4-2.png" is available in "png" format from:

<http://arxiv.org/ps/hep-ph/9411294v2>

This figure "fig1-3.png" is available in "png" format from:

<http://arxiv.org/ps/hep-ph/9411294v2>

This figure "fig2-3.png" is available in "png" format from:

<http://arxiv.org/ps/hep-ph/9411294v2>

This figure "fig3-3.png" is available in "png" format from:

<http://arxiv.org/ps/hep-ph/9411294v2>

($\Lambda=0.25$ GeV, $n_f=4$)

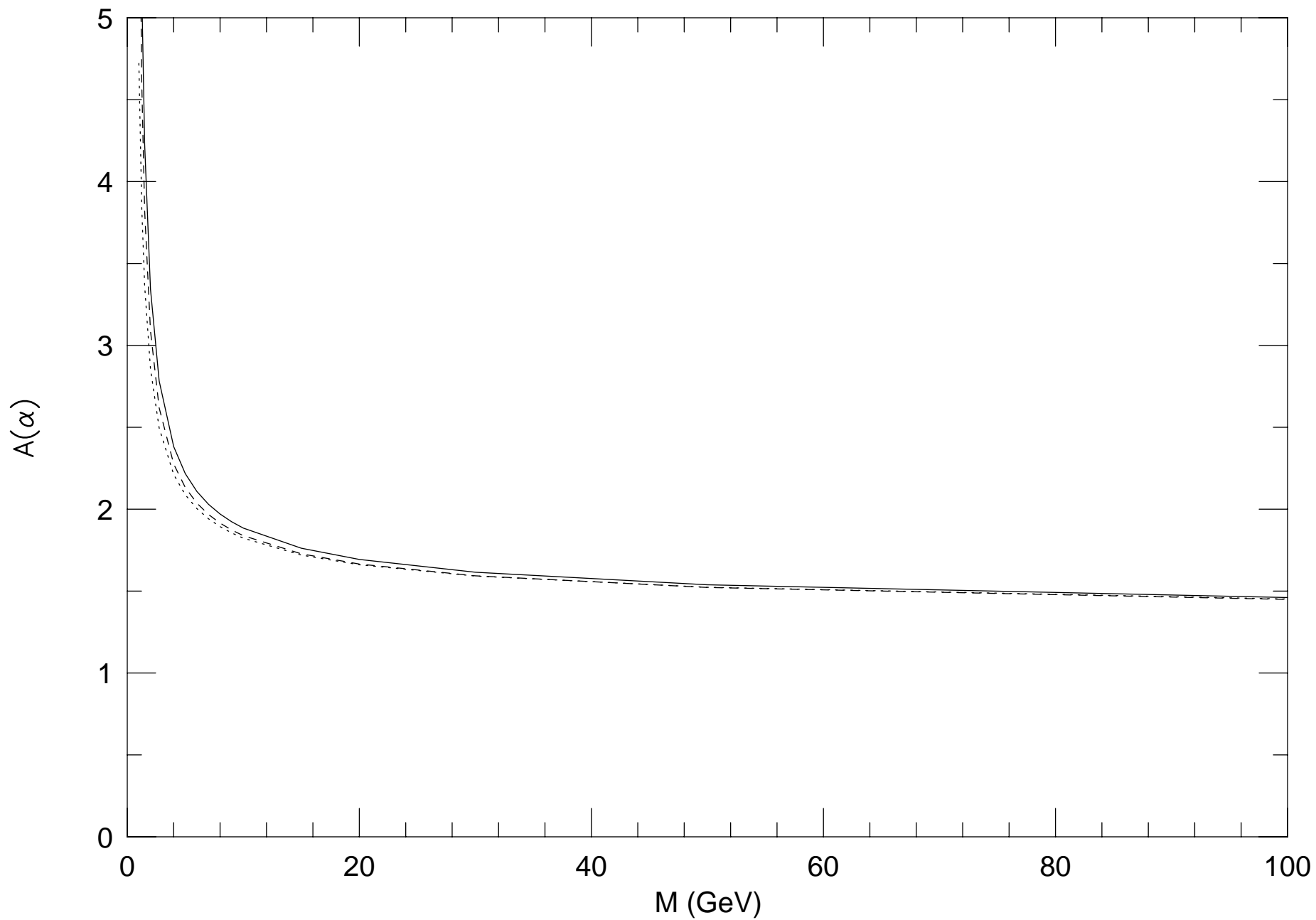


Fig. 3

This figure "fig4-3.png" is available in "png" format from:

<http://arxiv.org/ps/hep-ph/9411294v2>

This figure "fig1-4.png" is available in "png" format from:

<http://arxiv.org/ps/hep-ph/9411294v2>

This figure "fig2-4.png" is available in "png" format from:

<http://arxiv.org/ps/hep-ph/9411294v2>

This figure "fig3-4.png" is available in "png" format from:

<http://arxiv.org/ps/hep-ph/9411294v2>

This figure "fig4-4.png" is available in "png" format from:

<http://arxiv.org/ps/hep-ph/9411294v2>

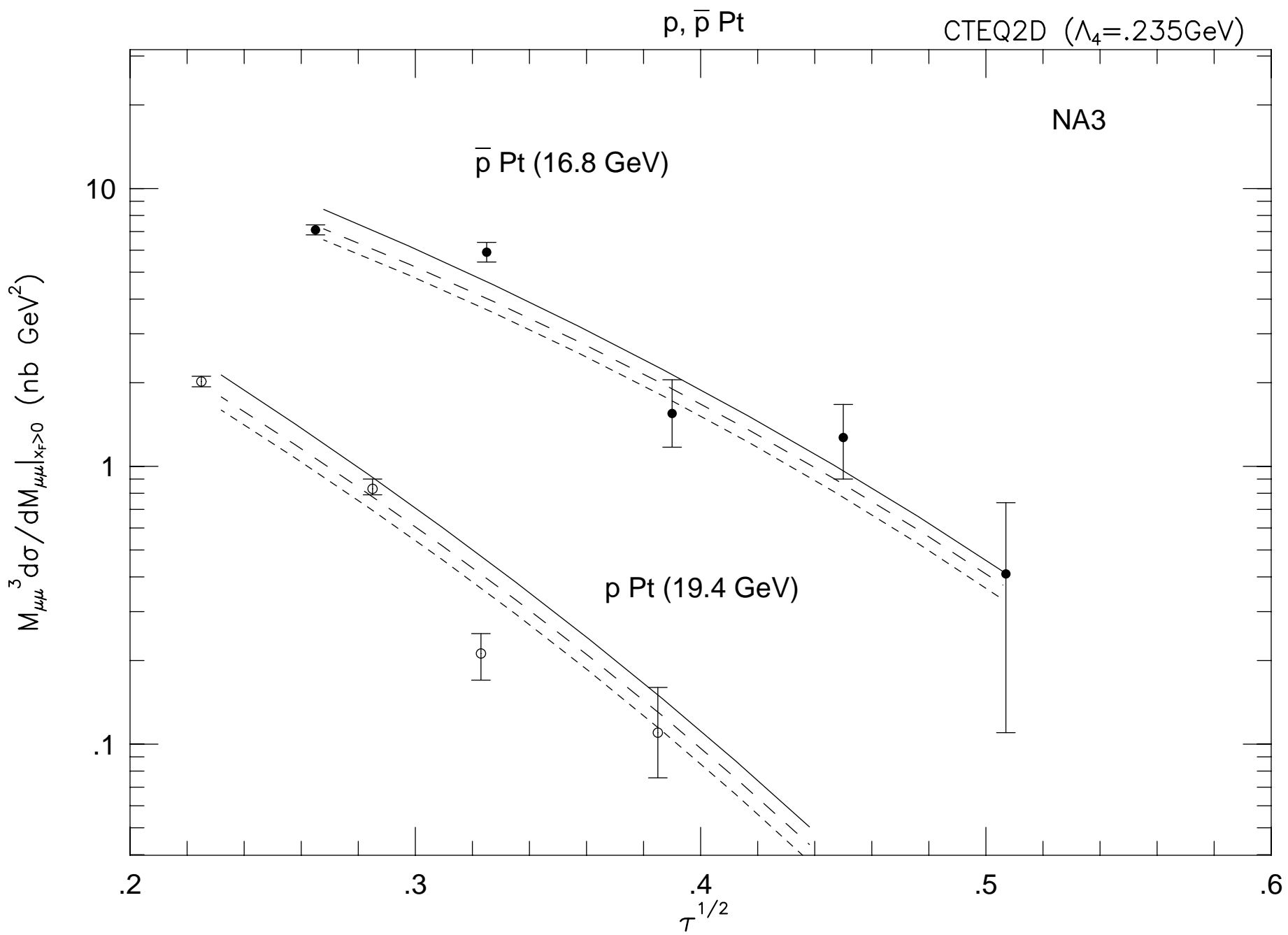


Fig. 4a

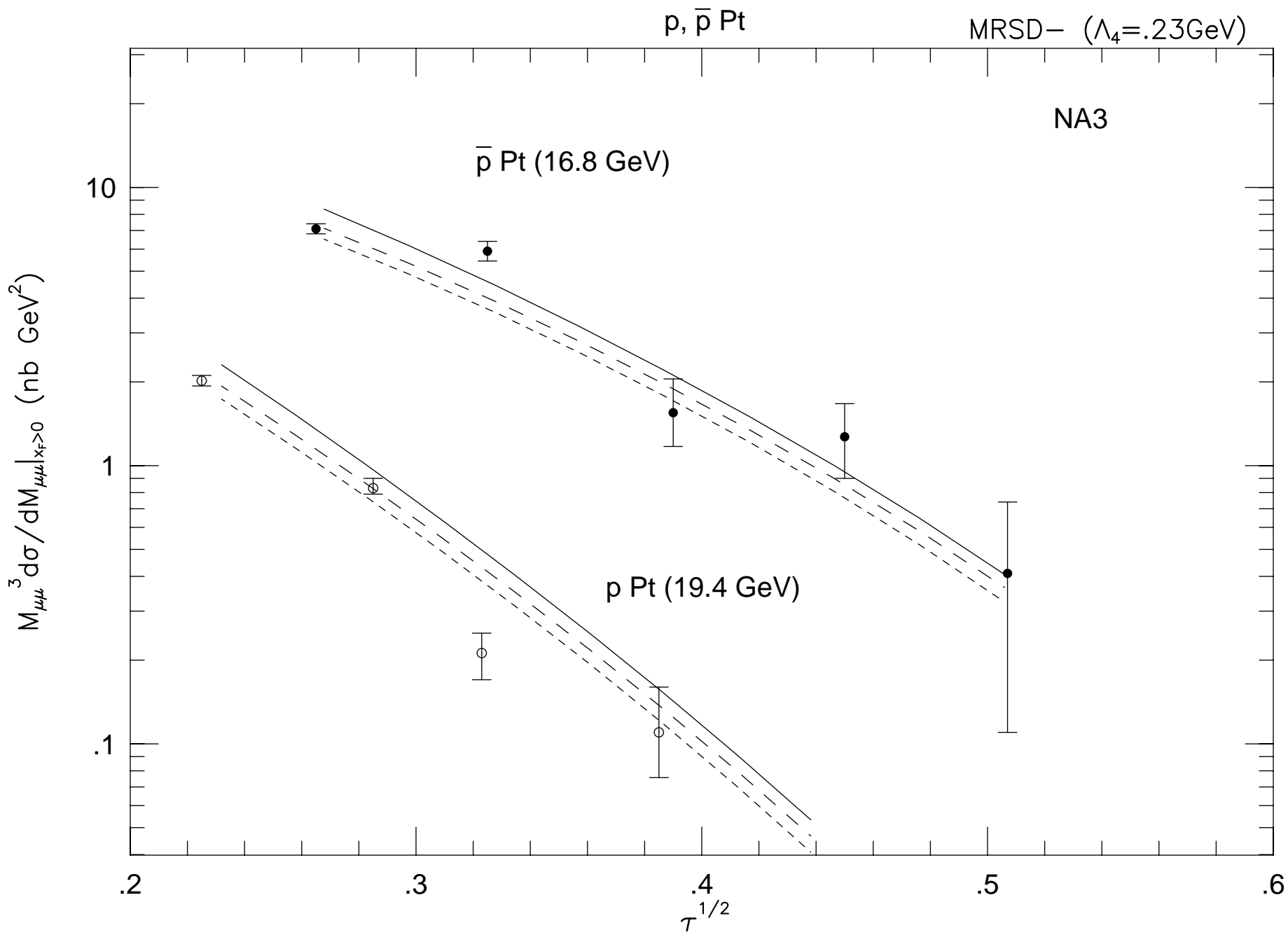


Fig. 4b

This figure "fig1-5.png" is available in "png" format from:

<http://arxiv.org/ps/hep-ph/9411294v2>

This figure "fig2-5.png" is available in "png" format from:

<http://arxiv.org/ps/hep-ph/9411294v2>

This figure "fig3-5.png" is available in "png" format from:

<http://arxiv.org/ps/hep-ph/9411294v2>

This figure "fig4-5.png" is available in "png" format from:

<http://arxiv.org/ps/hep-ph/9411294v2>

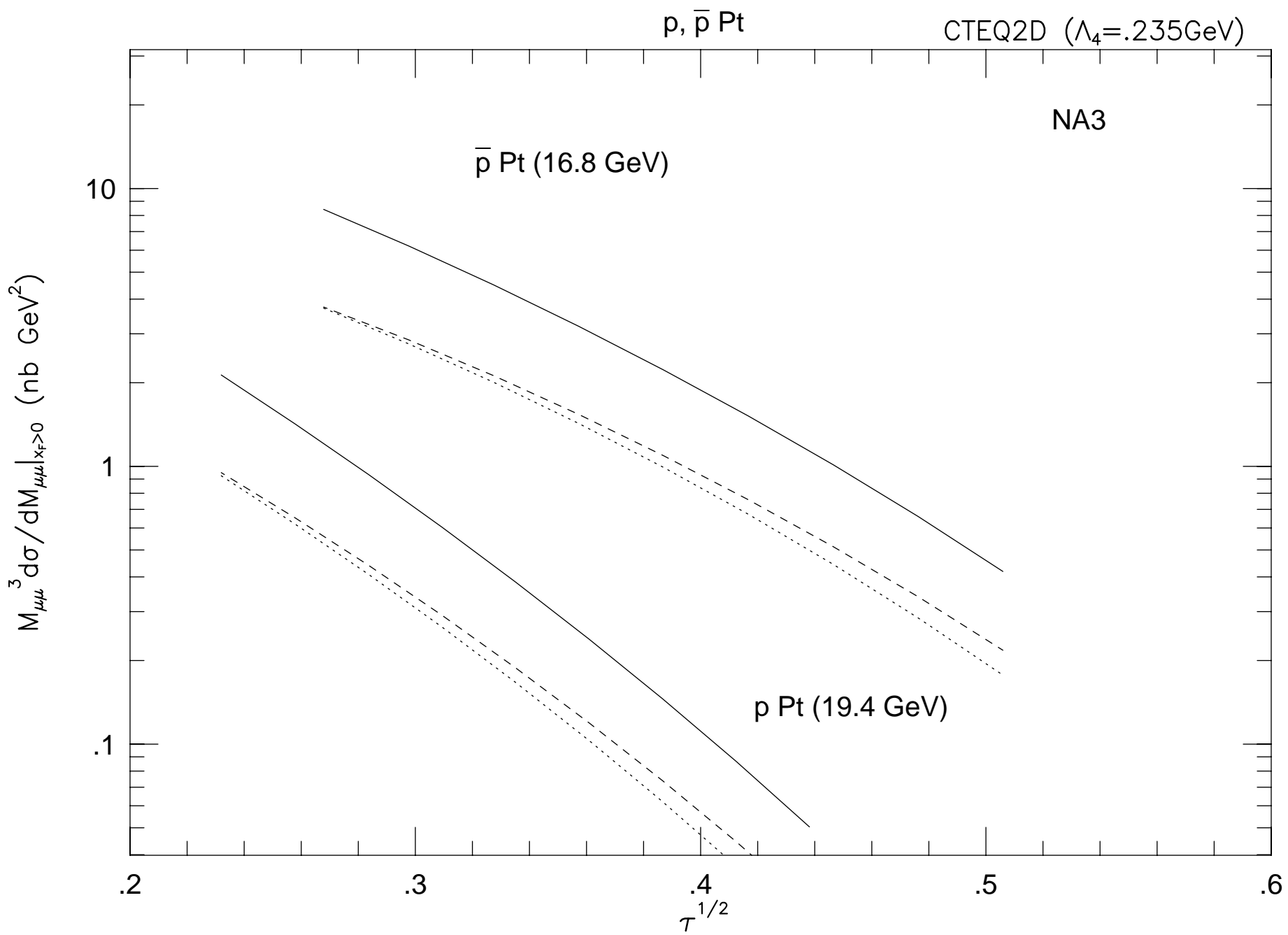


Fig. 5

This figure "fig1-6.png" is available in "png" format from:

<http://arxiv.org/ps/hep-ph/9411294v2>

This figure "fig2-6.png" is available in "png" format from:

<http://arxiv.org/ps/hep-ph/9411294v2>

This figure "fig3-6.png" is available in "png" format from:

<http://arxiv.org/ps/hep-ph/9411294v2>

This figure "fig4-6.png" is available in "png" format from:

<http://arxiv.org/ps/hep-ph/9411294v2>

p Pt (27.4 GeV)

CTEQ2D ($\Lambda_4=.235\text{GeV}$)

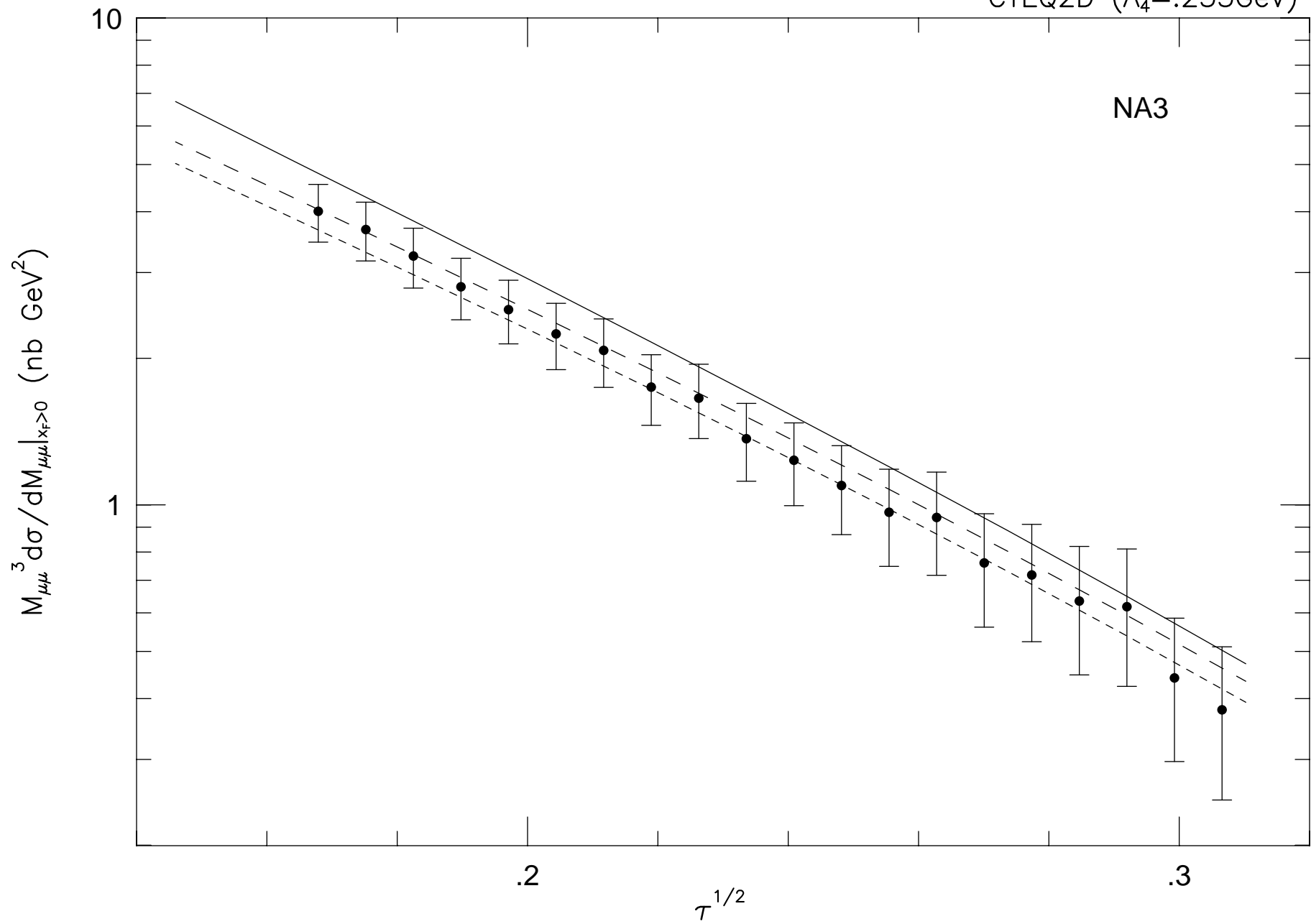


Fig. 6

$\bar{p} W (15.4 \text{ GeV})$

CTEQ2D ($\Lambda_4 = .235 \text{ GeV}$)

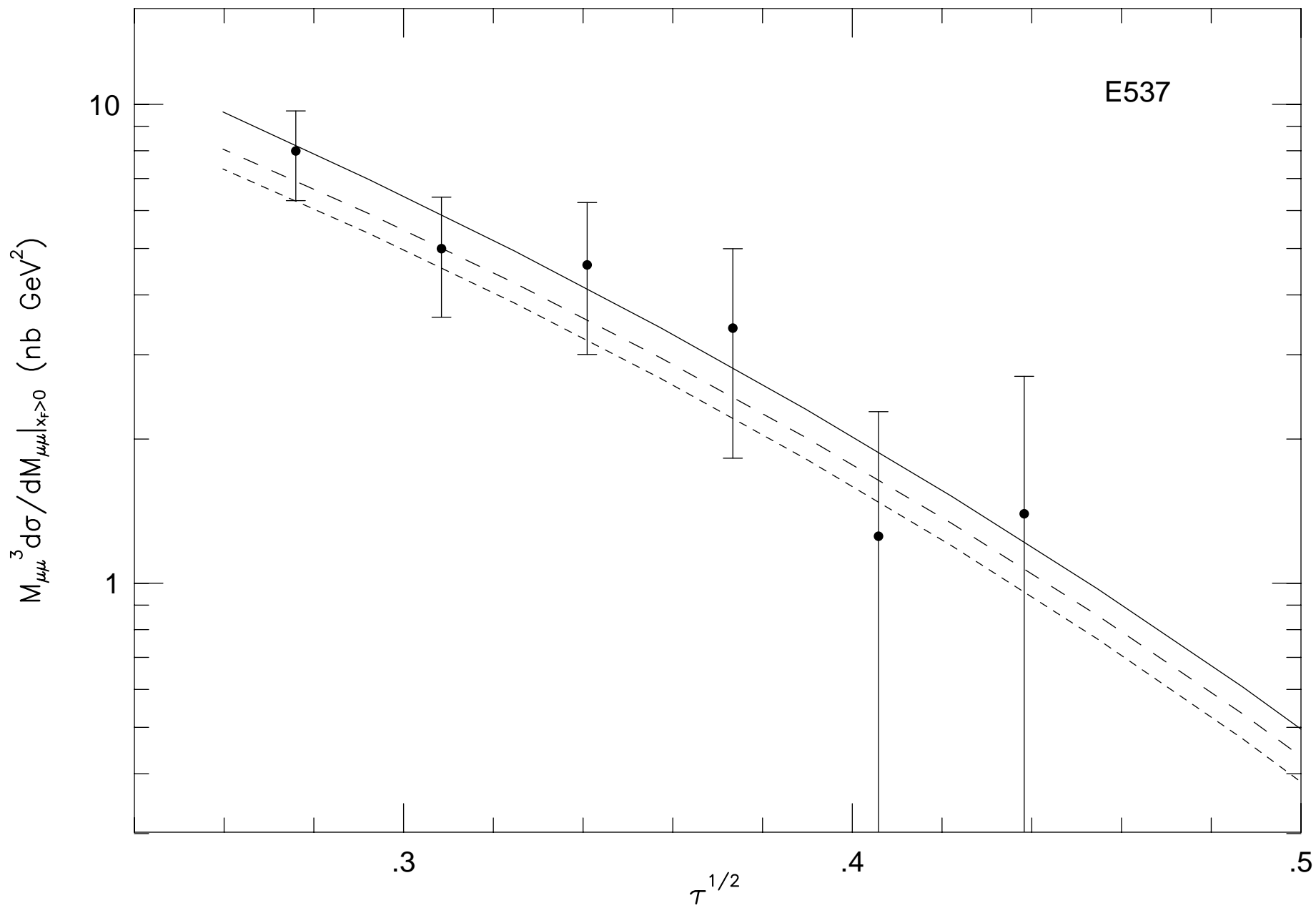


Fig. 7

$\bar{p} W (15.4 \text{ GeV})$

CTEQ2D ($\Lambda_4=0.235\text{GeV}$)

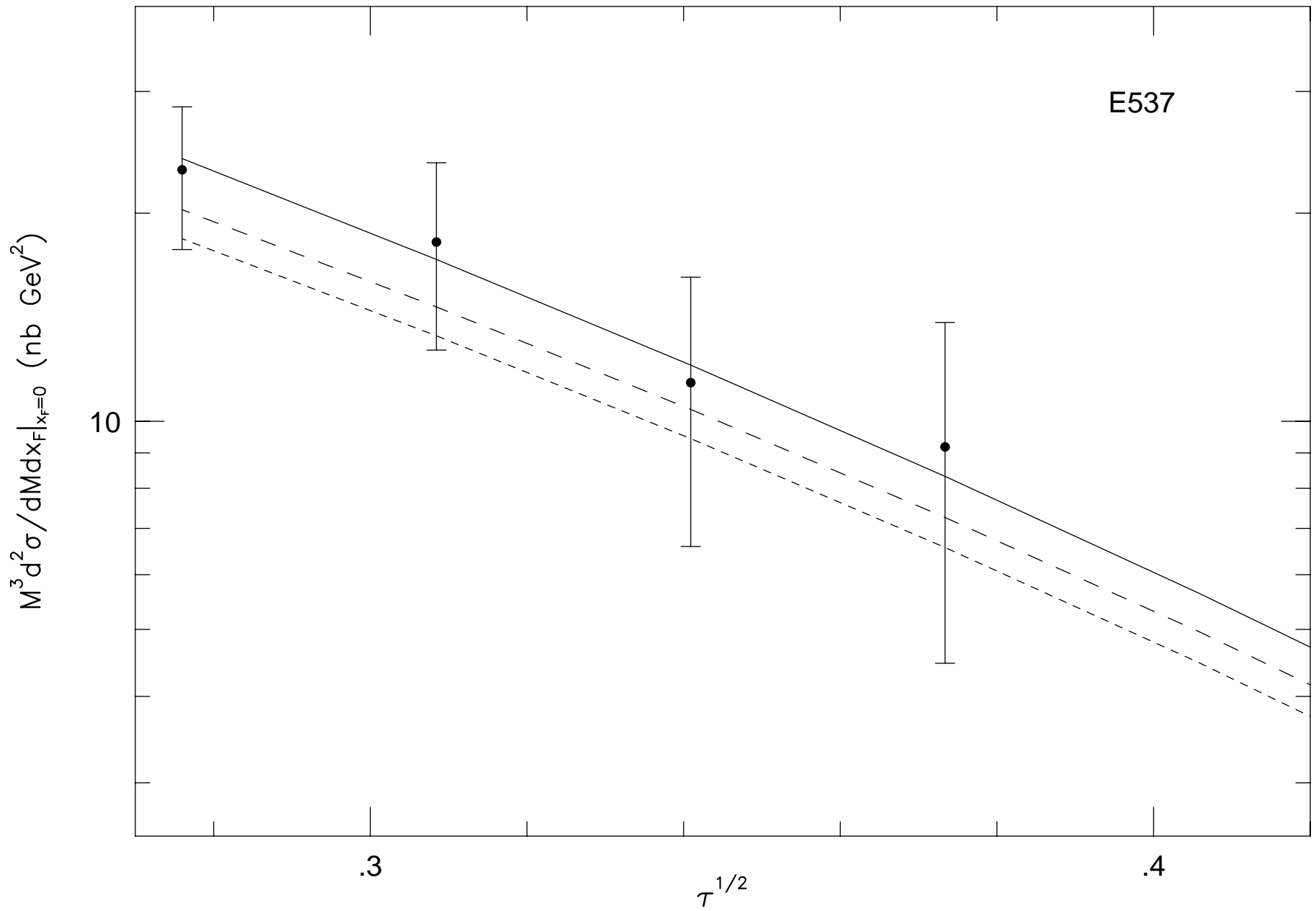


Fig. 8

p Cu (38.8 GeV)

CTEQ2D ($\Lambda_4=0.235\text{GeV}$)

E605

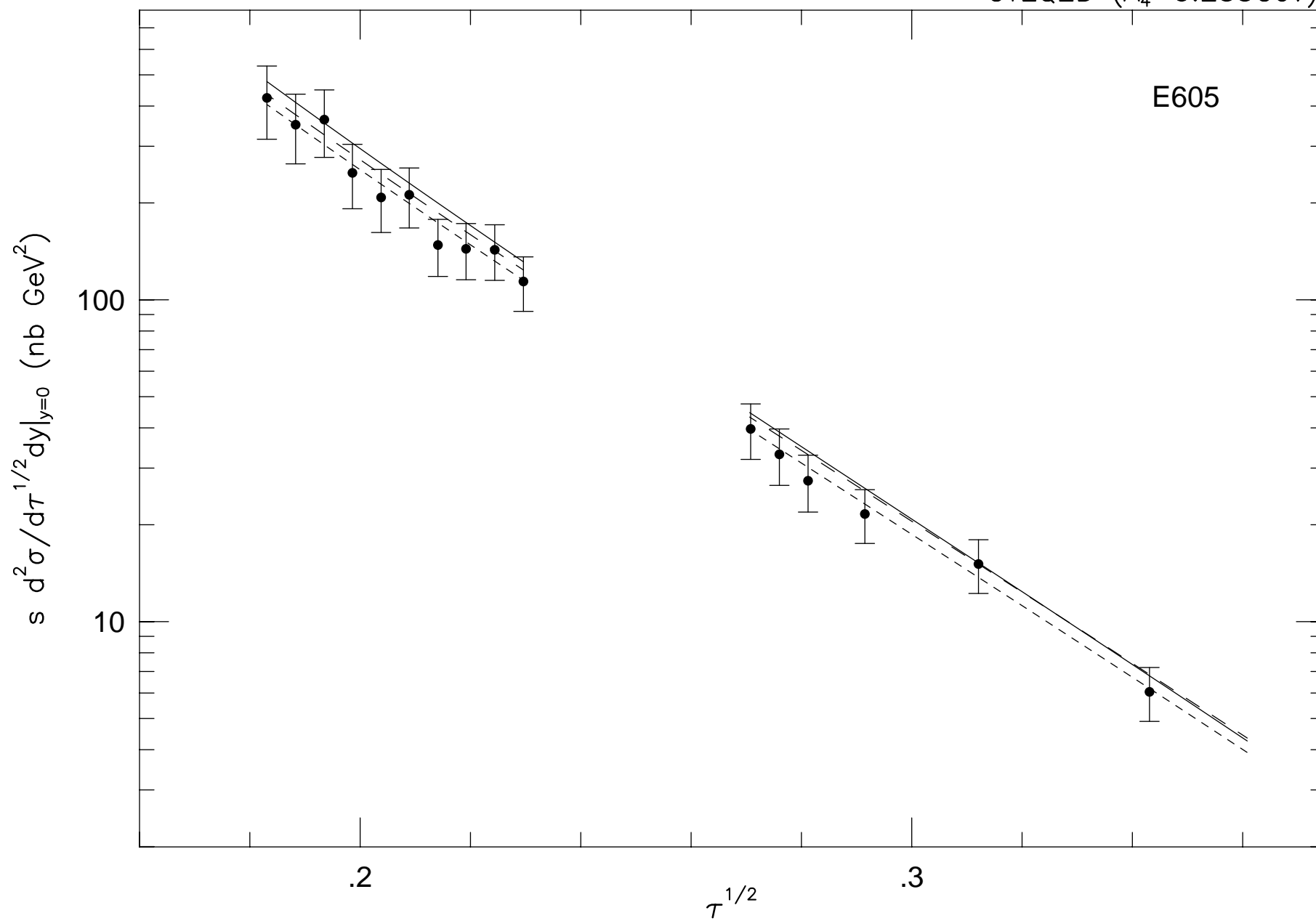


Fig. 9a

p Cu (38.8 GeV)

MRSD- ($\Lambda_4=0.23\text{GeV}$)

E605

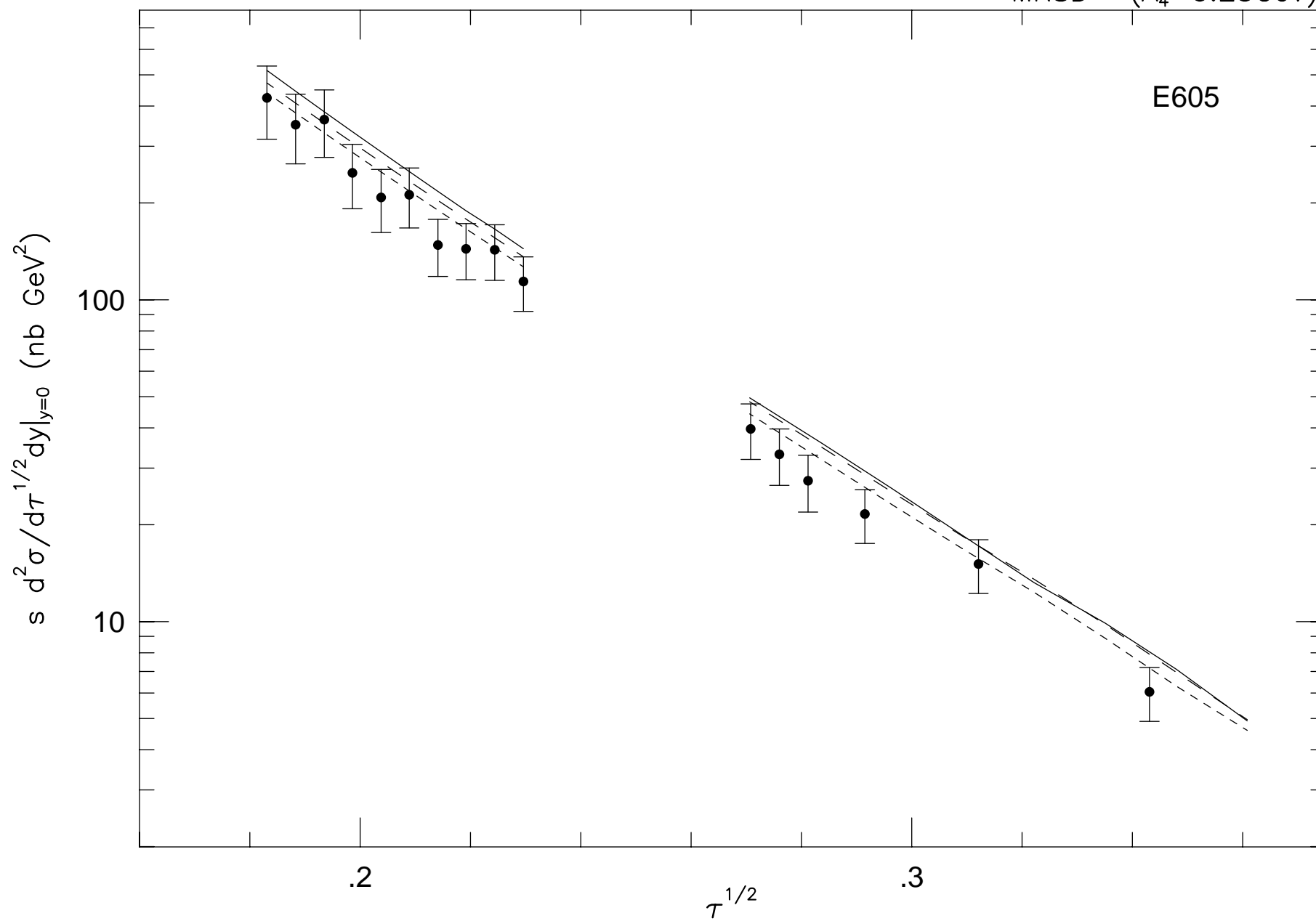


Fig. 9b

p ²H (38.8 GeV)

CTEQ2D ($\Lambda_4=.235\text{GeV}$)

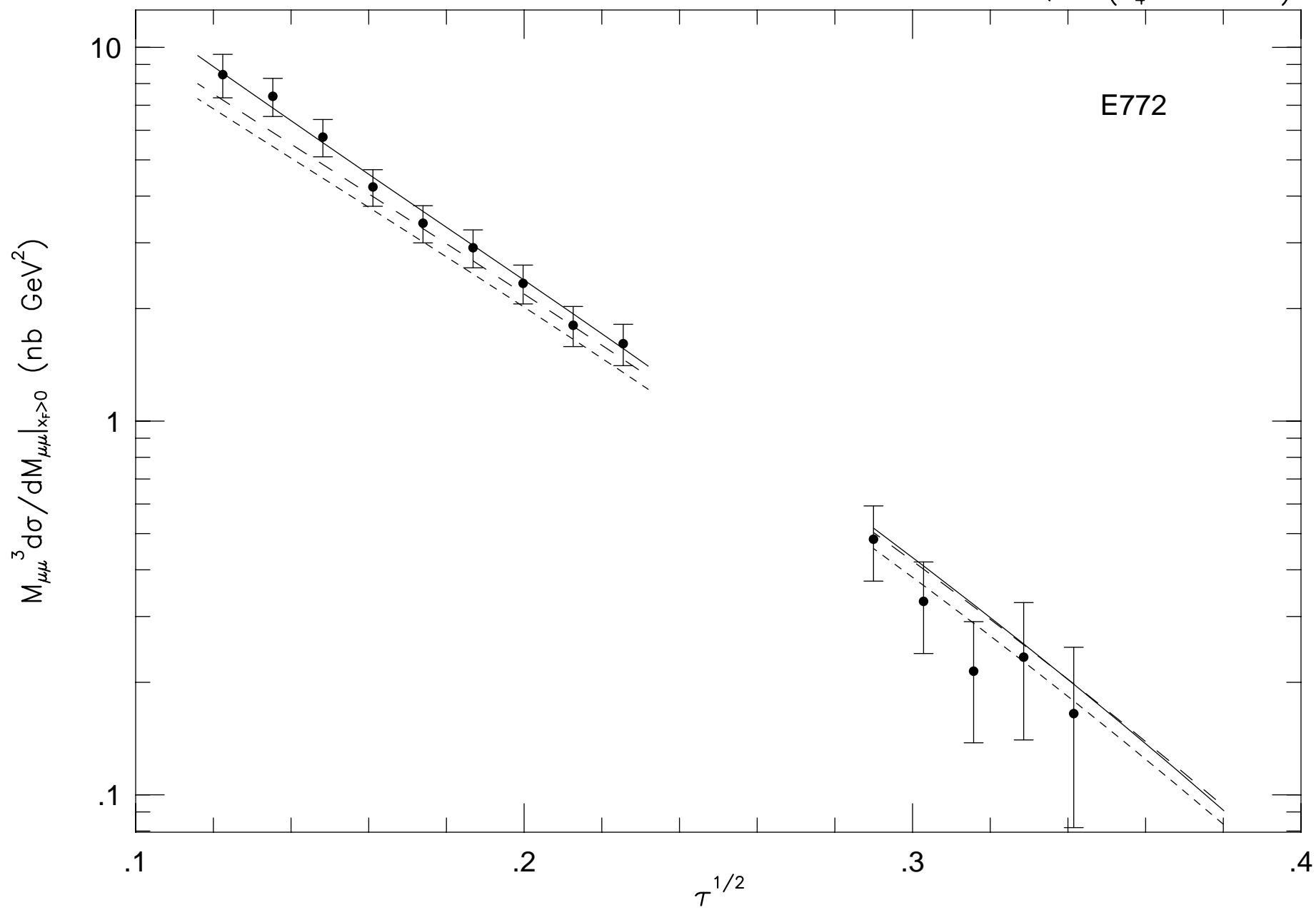


Fig. 10

p ²H (38.8 GeV)

CTEQ2D ($\Lambda_4=0.235\text{GeV}$)

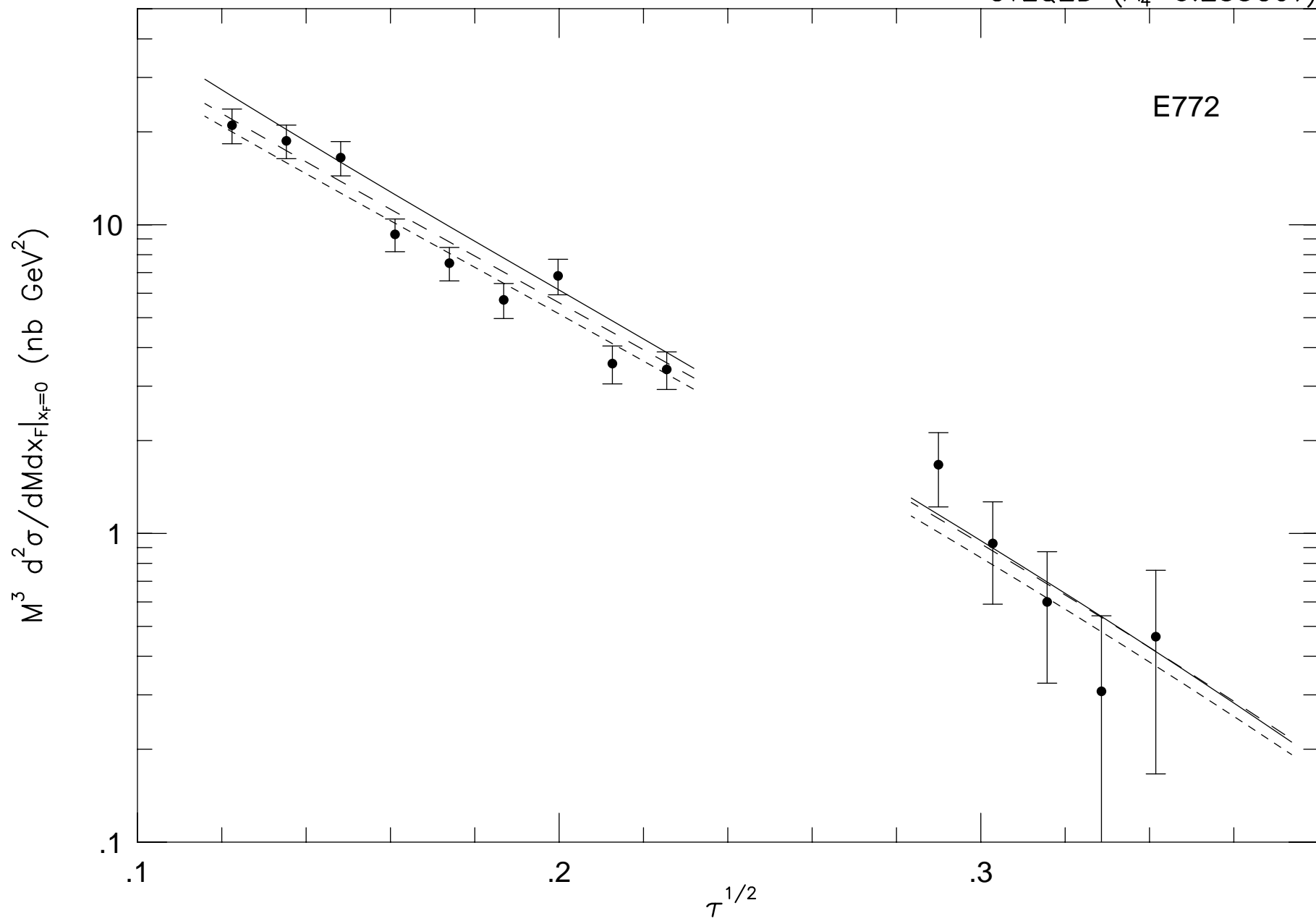


Fig. 11

$\bar{p} W (15.4 \text{ GeV})$

(CTEQ2D)

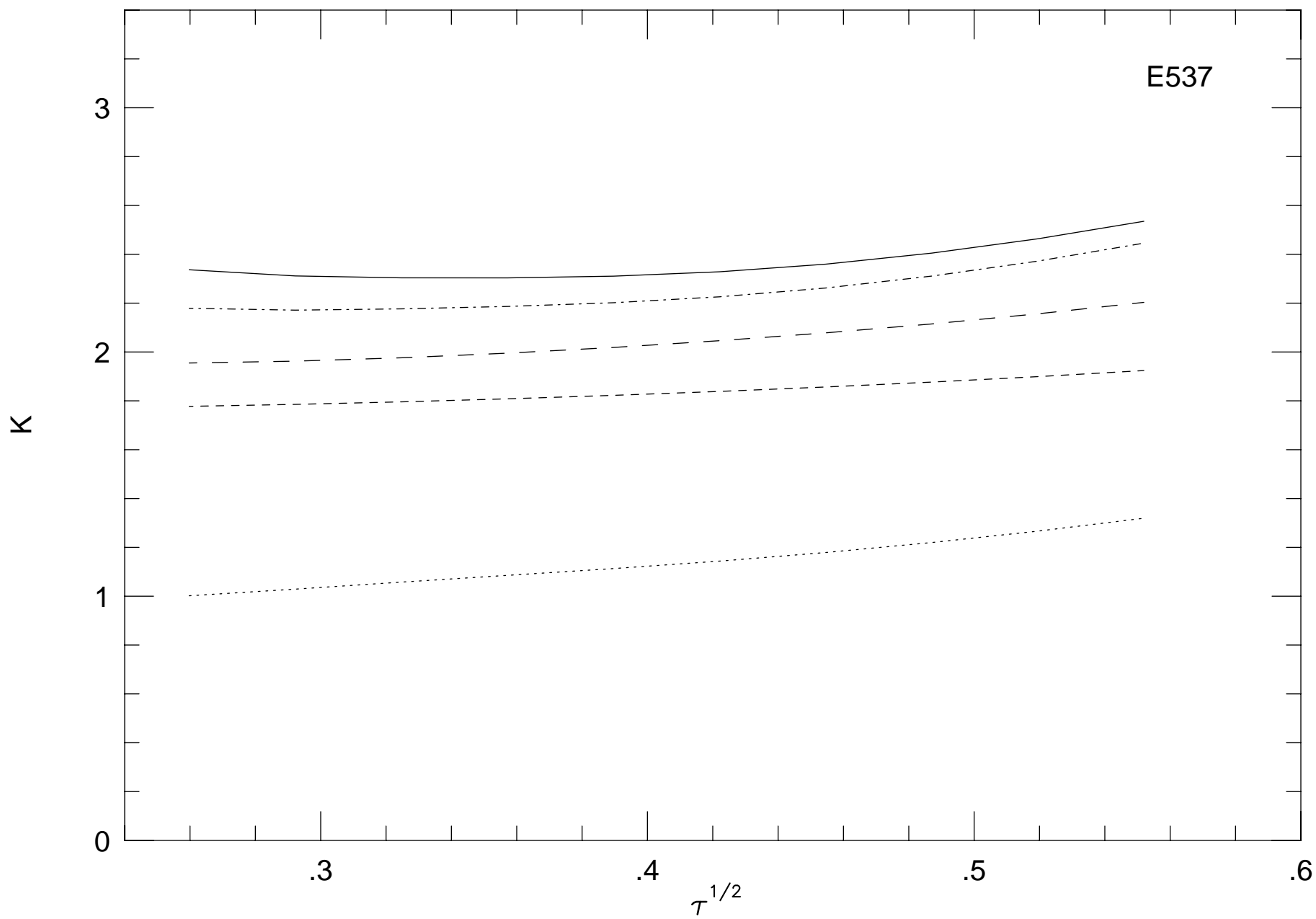


Fig. 12

p Pt (27.4 GeV)

($n_f=4$)

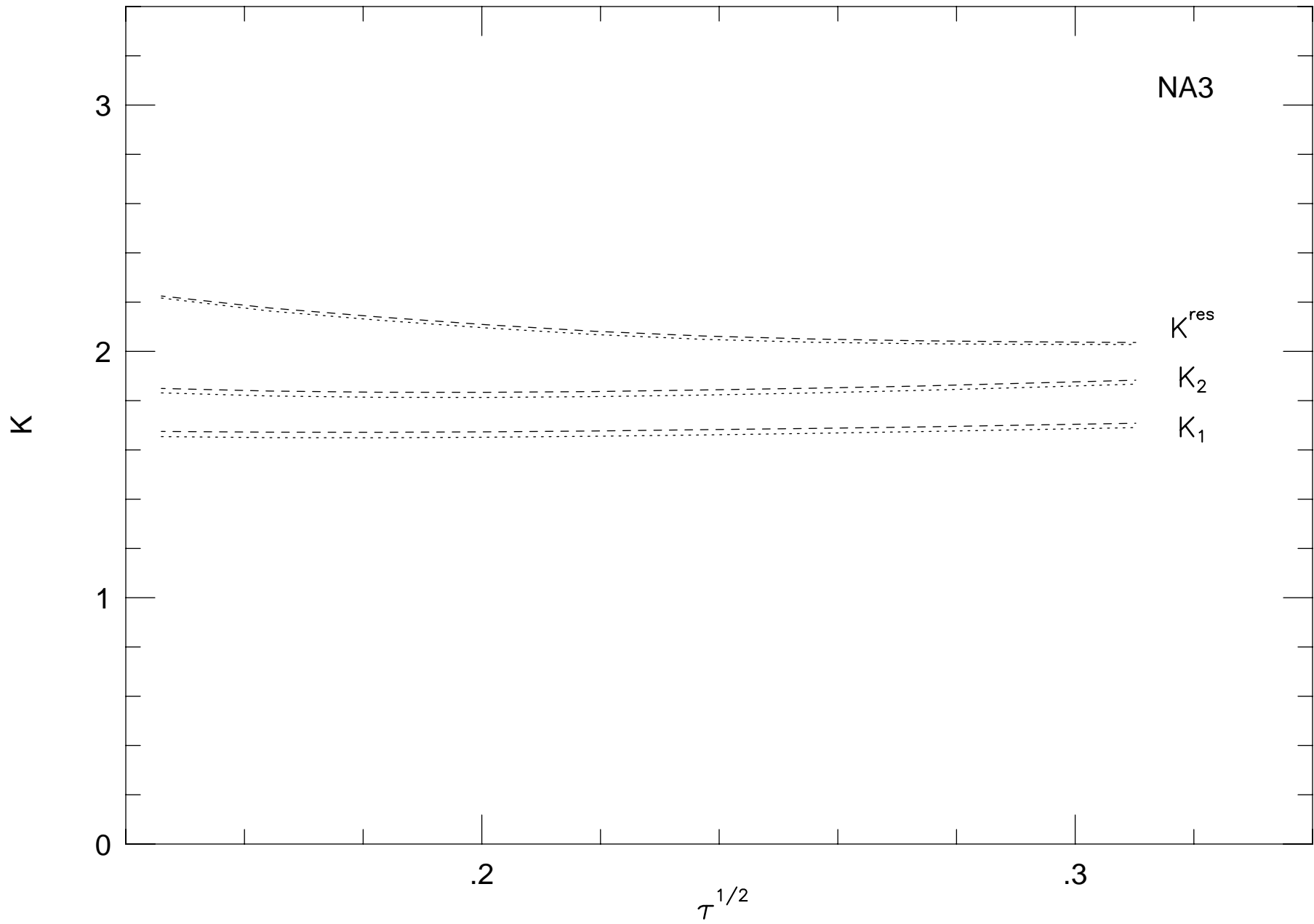


Fig. 13

p ²H (38.8 GeV)

(CTEQ2D)

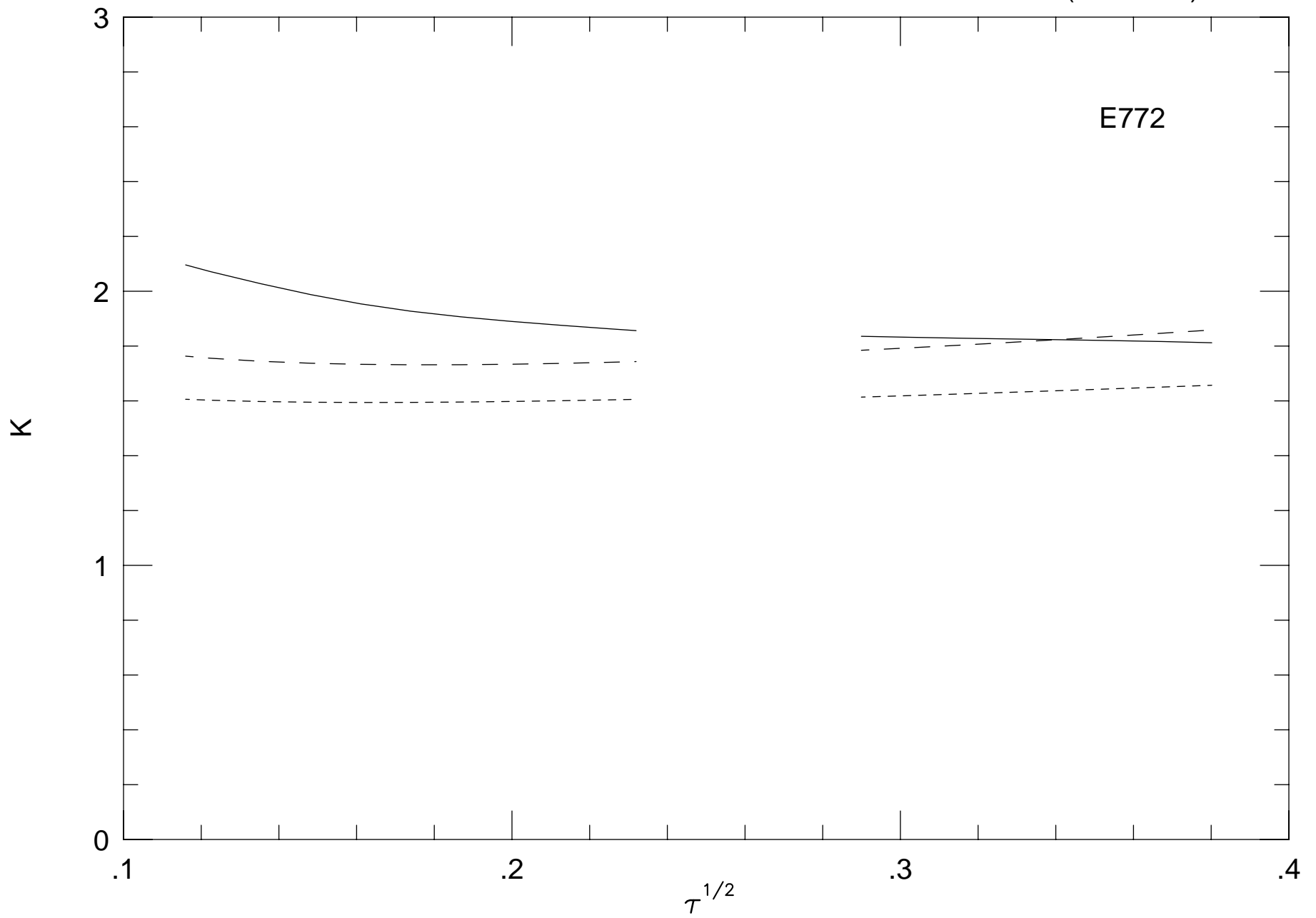


Fig. 14

p Cu (38.8 GeV)

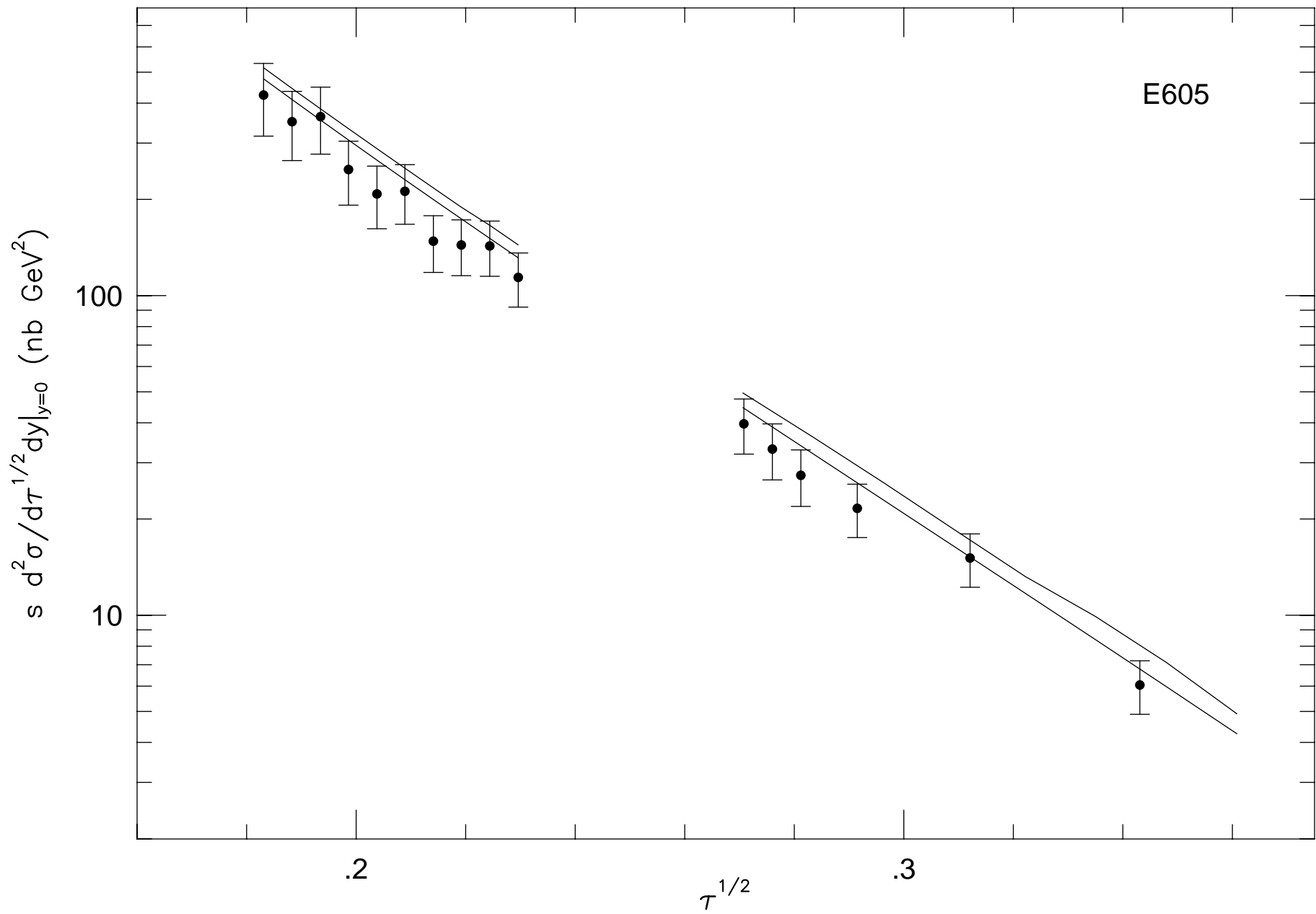


Fig. 15